Complete Separation of Deeply Virtual Photon and π^0 Electroproduction Observables of Unpolarized Protons

Carlos Muñoz Camacho*†

Los Alamos National Laboratory, Los Alamos, NM 87545, USA

Julie Roche†‡, P. King

Ohio University, Athens, OH 45701, USA

Charles E. Hyde-Wright†§, G. Gavalian, M. Amarian, S. Bültmann, M. Canan, G.E. Dodge, A. Radyushkin, L. Weinstein

Old Dominion University, Norfolk, VA 23529, USA

P.-Y. Bertin†‡, J. Ball, M. Brossard, R. de Masi, M. Garçon, F.-X. Girod, M. Guidal, H. S. Jo, M. MacCormick, B. Michel, S. Niccolai, B. Pire, S. Procureur, F. Sabatié, E. Voutier

LPC (Clermont) / LPSC (Grenoble) / IPNO (Orsay) / CPhT-Polytechnique (Palaiseau) / SPhN (Saclay) CEA/DSM/DAPNIA & CNRS/IN2P3, France

M. Mazouz

Faculté des Sciences de Monastir, Département de physique, 5000-Monastir, Tunisia

A. Camsonne, J.-P. Chen, E. Chudakov, A. Deur, D. Gaskell, J. Gomez, O. Hansen, D. Higinbotham, T. Horn, C. W. de Jager, J. LeRose, R. Michaels, S. Nanda, A. Saha, B. Wojtsekhowski

Thomas Jefferson National Accelerator Facility, Newport News, VA 23606, USA

X. Jiang, E. Kuchina, R. Ransome

Rutgers, The State University of New Jersey, Piscataway, NJ 08854, USA

* Contact person: munoz@jlab.org

† co-Spokesperson

‡ and Thomas Jefferson National Accelerator Facility, Newport News, VA 23606, USA

§ and Blaise Pascal University, Clermont-Ferrand, France

R. J. Feuerbach, V. Sulkosky

College of William and Mary, Williamsburg, VA 23187, USA

P. E. C. Markowitz

Florida International University, Miami, FL 33199, USA

A. Deshpande

Stony Brook University, Stony Brook, NY 11794, USA

P. Gueye

Hampton University, Hampton, VA 23668, USA

A. Kolarkar

University of Kentucky, Lexington, Kentucky 40506, USA

S. Širca

Dept. of Physics, University of Ljubljana, Slovenia

S. Choi, H.-Y. Kang, H. Kang, B. Lee, Y. Oh, J. Song

Seoul National University, Seoul 151-747, Korea

H.-J. Lu

Department of Modern Physics, University of Science and Technology of China, Hefei 230026, China

B. Craver, N. Liyanage, V. Nelyubin, M. Shabestari, X. Zheng

University of Virginia, Charlottesville, Virginia 22904, USA

R. Subedi

Kent State University, Kent, Ohio 44242, USA

L. Zhu

University of Illinois, Urbana, Illinois 61801, USA

Y. Qiang

Massachusetts Institute of Technology,

Cambridge, Massachusetts 02139, USA

H. Benaoum

Syracuse University, Syracuse, New York 13244, USA

F. Cusanno

INFN/Sezione Sanità, 00161 Roma, Italy

and

The Jefferson Lab Hall A Collaboration

(Dated: 11 December 2006, for JLab PAC31)

We propose to use the incident beam energy dependence of the Bethe-Heitler (BH) and deeply virtual Compton scattering (DVCS) amplitudes to isolate the BH·DVCS interference term from the pure DVCS^2 contribution to the photon electroproduction ($ep \to ep\gamma$) cross section in the deeply virtual regime. This is a necessary step in order to extract meaningful information about Generalized Parton Distributions (GPDs) through DVCS cross sections. The understanding of the pure DVCS contribution to the cross section is essential in order to plan future 12 GeV DVCS measurements, some of which were already approved by PAC30. In order to measure the size of the pure DVCS contribution to the electroproduction cross section, we request 400 h of beam time (plus 6 additional days for calorimeter calibration and optical curing), with a total of three different beam energies. This beam time will also allow the measurement of the 5 response functions of the exclusive deep virtual π^0 channel, in particular $d\sigma_L$ and $d\sigma_T$ by a conventional Rosenbluth separation. This separation, as a function of Q^2, is essential for testing the factorization of $d\sigma_L$ in the deeply virtual $ep \to ep\pi^0$ reaction.

Contents

I. INTRODUCTION AND MOTIVATION

Deeply virtual Compton scattering (DVCS) refers to the reaction $ep \to ep\gamma$ in the Bjorken limit of Deep Inelastic Scattering (DIS). DVCS is the simplest probe of a new class of light-cone (quark) matrix elements, called Generalized Parton Distributions (GPDs). The GPDs offer the exciting possibility of the first ever spatial images of the quark waves inside the proton, as a function of their wavelength. The correlation of transverse spatial and longitudinal momentum information contained in the GPDs provides a new tool to evaluate the contribution of quark orbital angular momentum to the proton spin.

We propose precision measurements of the beam helicity-dependent and helicity-independent cross sections for the $ep \to ep\gamma$ and $ep \to ep\pi^0$ reactions in exclusive deeply virtual kinematics. We will use our successful technique from the 5.75 GeV Hall A DVCS experiment (E00-110) [1]. With polarized 6.0, 4.8 and 3.6 GeV beams incident on the liquid hydrogen target, we will detect the scattered electron in the Hall A HRS-L spectrometer and the emitted photon in an expanded PbF_2 calorimeter. With a new digital trigger on the PbF_2 calorimeter, we will be able to run at higher luminosity with greater acceptance for triggering on asymmetric π^0 decays.

In the photon electroproduction cross section, the DVCS amplitude interferes coherently with the Bethe-Heitler (BH) amplitude (see Fig. 1). DVCS scaling is predicted [2, 3] as a function of Q^2 for $Q^2 \gg \Lambda^2_{\rm QCD}$ at x_B fixed and $-t = -\Delta^2 = -(q-q')^2 \ll Q^2$. In E00-110, we measured the t-dependence of the imaginary part of the BH·DVCS interference for $Q^2 = 1.5$, 1.9, and 2.3 GeV^2, at $x_B = 0.36$. These data give strong evidence for the dominance of the leading twist (GPD) term in the imaginary part of the DVCS amplitude. However, due to the π^0 background, we were able to measure the real part of the BH·DVCS interference only at $Q^2 = 2.3$ GeV^2. With the expanded calorimeter and upgraded trigger, we will be able to test the twist-2 dominance in the real part of the DVCS amplitude, also.

Ever since DVCS was first proposed as a way to access GPDs [2, 3], it has been a general belief in the community that at JLab and HERMES kinematics, the DVCS^2 contribution to the cross section would be small compared to the Bethe-Heitler cross section, and therefore any experimental deviations from the BH cross section could be attributed purely to the BH·DVCS interference terms. The limited statistics of previous DVCS measurements (and the concomitant integration over large kinematic bins) in non-dedicated experiments could

not test this assumption. E00-110 provided the first purely experimental information that the DVCS^2 contribution to the cross section *might* be important. This experimental evidence is also supported with theoretical model calculations of the DVCS^2 term.

In summary, the experimental goals of this proposal are :

- To separate the pure DVCS^2 contribution to the photon electroproduction cross section. To do so, the DVCS cross section will be measured at fixed $x_B = 0.36$ and three Q^2= 2.3, 1.9, 1.5 GeV^2 using two different beam energies at each Q^2.

- To measure the Q^2 dependence of the unpolarized DVCS cross section. Let us remember that the goal of E00-110 was to measure the difference of the polarized cross sections in order to obtain the imaginary part of the DVCS·BH interference and it was successful doing so. In addition, we have measured with very high accuracy the unpolarized cross section at Q^2=2.3 GeV^2. This proposal will complete this previous measurement by measuring the same quantity at the other two Q^2 settings 1.9 and 1.5 GeV^2. In section IV C we will explain the modifications needed in our electronics to obtain this result.

- To perform a full separation of the five response functions of the π^0 electroproduction (unpolarized target) in this kinematic regime. This analysis results directly from our upgraded trigger for π^0 events, and running at two beam energies for each Q^2 point. Measurements of the Q^2 dependence of the separated longitudinal cross section, $d\sigma_L$, are essential for testing the approach to factorization in the $ep \rightarrow ep\pi^0$ channel.

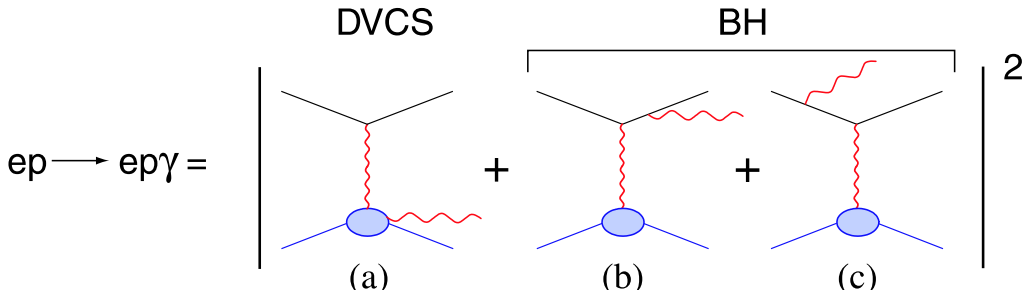

FIG. 1: Lowest order QED diagrams for the process $ep \rightarrow ep\gamma$, including the DVCS (a) and the Bethe-Heitler (b, c) amplitudes.

II. DEEP PHOTON ELECTROPRODUCTION

The photon electroproduction cross section of a polarized lepton beam of energy k off an unpolarized target of mass M is sensitive to the coherent interference of the DVCS amplitude with the Bethe-Heitler amplitude (see Fig. 1). It can be written as:

$$\begin{aligned}
\frac{d^5\sigma(\lambda,\pm e)}{d^5\Phi} &= \frac{d\sigma_0}{dQ^2dx_B}\left|\mathcal{T}^{BH}(\lambda)\pm\mathcal{T}^{DVCS}(\lambda)\right|^2/|e|^6 \\
&= \frac{d\sigma_0}{dQ^2dx_B}\left[\left|\mathcal{T}^{BH}(\lambda)\right|^2+\left|\mathcal{T}^{DVCS}(\lambda)\right|^2\mp\mathcal{I}(\lambda)\right]\frac{1}{e^6} \qquad (1)\\
\frac{d\sigma_0}{dQ^2dx_B} &= \frac{\alpha^3_{\rm QED}}{16\pi^2(s_e-M^2)^2x_B}\frac{1}{\sqrt{1+\epsilon^2_{DVCS}}} \qquad (2)\\
\epsilon^2_{DVCS} &= 4M^2x_B^2/Q^2 \\
s_e &= 2Mk+M^2
\end{aligned}$$

where $d^5\Phi = dQ^2dx_Bd\phi_edtd\phi_{\gamma\gamma}$, λ is the electron helicity and the $+(-)$ stands for the sign of the charge of the lepton beam. The BH contribution is calculable in QED, given our $\approx 1\%$ knowledge of the proton elastic form factors at small momentum transfer. The other two contributions to the cross section, the interference and the DVCS^2 terms, provide complementary information on GPDs. It is possible to exploit the structure of the cross section as a function of the angle $\phi_{\gamma\gamma}$ between the leptonic and hadronic plane to separate up to a certain degree the different contributions to the total cross section [4]. The angular separation can be supplemented by an energy separation. This energy separation is the main goal of this proposal and is detailed in section II B.

The $|\mathcal{T}^{BH}|^2$ term is given in [5], Eq. (25), and only its general form is reproduced here:

$$|\mathcal{T}^{BH}|^2 = \frac{e^6}{x_B^2ty^2(1+\epsilon^2_{DVCS})^2\mathcal{P}_1(\phi_{\gamma\gamma})\mathcal{P}_2(\phi_{\gamma\gamma})}\sum_{n=0}^{2}c_n^{BH}\cos(n\phi_{\gamma\gamma}) \qquad (3)$$

The harmonic terms c_n^{BH} depend upon bilinear combinations of the ordinary elastic form factors $F_1(t)$ and $F_2(t)$ of the proton. The factors $\mathcal{P}_i$ are the electron propagators in the BH

amplitude:

$$\mathcal{P}_1(\phi_{\gamma\gamma}) = (k-q')^2/Q^2 \;=\; -\left[J + 2K\cos\phi_{\gamma\gamma}\right] / \left[y(1+\epsilon^2_{DVCS})\right] \tag{4}$$

$$\mathcal{P}_2(\phi_{\gamma\gamma}) = (k'-q')^2/Q^2 \;=\; 1 + \frac{t}{Q^2} + \left[J + 2K\cos\phi_{\gamma\gamma}\right] / \left[y(1+\epsilon^2_{DVCS})\right] \tag{5}$$

$$J \;=\; \left[1 - y - y\epsilon^2_{DVCS}/2\right]\left[1 + \mathcal{O}(t/Q^2)\right] \tag{6}$$

$$K \;=\; \frac{t_{\min} - t}{Q^2}\left[1 - x_B\right]\left[1 - y\right]\left[1 + \mathcal{O}(t/Q^2)\right]. \tag{7}$$

The last two lines show the simplified forms in the Bjorken limit.

A. Harmonic structure and parametrization in term of GPDs

The interference term is a linear combination of GPDs, whereas the DVCS^2 term is a bilinear combination of GPDs:

$$\mathcal{I} \;=\; \frac{e^6}{x_B y^3 \mathcal{P}_1(\phi_{\gamma\gamma})\mathcal{P}_2(\phi_{\gamma\gamma}) t}\left\{c_0^{\mathcal{I}} + \sum_{n=1}^{3}(-1)^n\left[c_n^{\mathcal{I}}(\lambda)\cos(n\phi_{\gamma\gamma}) - \lambda s_n^{\mathcal{I}}\sin(n\phi_{\gamma\gamma})\right]\right\} \tag{8}$$

$$\left|\mathcal{T}^{DVCS}(\lambda)\right|^2 \;=\; \frac{e^6}{y^2Q^2}\left\{c_0^{DVCS} + \sum_{n=1}^{2}(-1)^n c_n^{DVCS}\cos(n\phi_{\gamma\gamma}) + \lambda s_1^{DVCS}\sin(\phi_{\gamma\gamma})\right\} \tag{9}$$

The Fourier coefficients $c_n^{\mathcal{I}}$ and $s_n^{\mathcal{I}}$ of the interference term are:

$$\begin{aligned}
c_0^{\mathcal{I}} \;&=\; -8(2-y)\Re\mathrm{e}\left\{\frac{(2-y)^2}{1-y}K^2\mathcal{C}^{\mathcal{I}}(\mathcal{F}) + \frac{t}{Q^2}(1-y)(1-x_B)\left[\mathcal{C}^{\mathcal{I}} + \Delta\mathcal{C}^{\mathcal{I}}\right](\mathcal{F})\right\} \\
\begin{Bmatrix} c_1^{\mathcal{I}} \\ \lambda s_1^{\mathcal{I}} \end{Bmatrix} \;&=\; -8K\begin{Bmatrix} (2-2y+y^2) \\ -\lambda y(2-y) \end{Bmatrix}\begin{Bmatrix} \Re\mathrm{e} \\ \Im\mathrm{m} \end{Bmatrix}\mathcal{C}^{\mathcal{I}}(\mathcal{F}) \\
\begin{Bmatrix} c_2^{\mathcal{I}} \\ \lambda s_2^{\mathcal{I}} \end{Bmatrix} \;&=\; \frac{-16K^2}{2-x_B}\begin{Bmatrix} (2-y) \\ -\lambda y \end{Bmatrix}\begin{Bmatrix} \Re\mathrm{e} \\ \Im\mathrm{m} \end{Bmatrix}\mathcal{C}^{\mathcal{I}}(\mathcal{F}^{\mathrm{eff}})
\end{aligned} \tag{10}$$

The Fourier coefficients $c_3^{\mathcal{I}}$, $s_3^{\mathcal{I}}$ are gluon transversity terms. We expect these to be very small in our kinematics, and thus our Fourier analysis in $\phi_{\gamma\gamma}$ will yield only an upper bound. It would be exciting if they generated a measurable signal. The $\mathcal{C}^I$ and $\Delta\mathcal{C}^I$ amplitudes are the angular harmonic terms defined in Eqs. (69) and (72) of [5] (we have suppressed the subscript "unp" since our measurements are only with an unpolarized target). These angular harmonics depend on the interference of the BH amplitude with the set $\mathcal{F} = \{\mathcal{H}, \mathcal{E}, \tilde{\mathcal{H}}, \tilde{\mathcal{E}}\}$

of twist-2 Compton form factors (CFFs) or the related set $\mathcal{F}^{\rm eff}$ of effective twist-3 CFFs:

$$\mathcal{C}^I(\mathcal{F}) = F_1(t)\mathcal{H}(\xi,t) + \xi G_M(t)\tilde{\mathcal{H}}(\xi,t) - \frac{t}{4M^2}F_2(t)\mathcal{E}(\xi,t) \quad (11)$$

$$\mathcal{C}^I(\mathcal{F}^{\rm eff}) = F_1(t)\mathcal{H}^{\rm eff}(\xi,t) + \xi G_M(t)\tilde{\mathcal{H}}^{\rm eff}(\xi,t) - \frac{t}{4M^2}F_2(t)\mathcal{E}^{\rm eff}(\xi,t) \quad (12)$$

$$\left[\mathcal{C}^I + \Delta\mathcal{C}^I\right](\mathcal{F}) = F_1(t)\mathcal{H}(\xi,t) - \frac{t}{4M^2}F_2(t)\mathcal{E}(\xi,t) - \xi^2 G_M(t)\left[\mathcal{H}(\xi,t) + \mathcal{E}(\xi,t)\right]. \quad (13)$$

The usual proton elastic form factors, F_1, F_2 and $G_M = F_1 + F_2$ are defined to have negative arguments in the space-like regime. The Compton form factors are defined in terms of the vector GPDs H and E, and the axial vector GPDs $\tilde{H}$ and $\tilde{E}$. For example ($f \in \{u,d,s\}$) [5]:

$$\mathcal{H}(\xi,t) = \sum_f \left[\frac{e_f}{e}\right]^2 \Bigg\{ i\pi \left[H_f(\xi,\xi,t) - H_f(-\xi,\xi,t)\right] + \mathcal{P}\int_{-1}^{+1} dx \left[\frac{1}{\xi - x} - \frac{1}{\xi + x}\right] H_f(x,\xi,t)\Bigg\}. \quad (14)$$

Thus, the imaginary part accesses a linear combination of GPDs at $x = \pm\xi$, whereas the real part probes GPD integrals over x.

The bilinear DVCS Fourier coefficients are:

$$c_0^{\rm DVCS} = 2(2 - 2y + y^2)\mathcal{C}^{DVCS}(\mathcal{F},\mathcal{F}^*)$$

$$\begin{Bmatrix} c_1^{\rm DVCS} \\ \lambda s_1^{DVCS} \end{Bmatrix} = \frac{8K}{2 - x_B}\begin{Bmatrix} 2 - y \\ -\lambda y \end{Bmatrix}\begin{Bmatrix} \Re{\rm e} \\ \Im{\rm m} \end{Bmatrix}\mathcal{C}^{\rm DVCS}(\mathcal{F}^{eff},\mathcal{F}^*) \quad (15)$$

The $c_2^{\rm DVCS}$ coefficient is again a gluon transversity term.

The only twist-2 DVCS angular harmonic term is:

$$\mathcal{C}^{DVCS}(\mathcal{F},\mathcal{F}^*) = \frac{1}{(2 - x_B)^2}\Big\{4(1 - x_B)\left(\mathcal{H}\mathcal{H}^* + \tilde{\mathcal{H}}\tilde{\mathcal{H}}^*\right) - x_B^2 2\Re{\rm e}\left[\mathcal{H}\mathcal{E}^* + \tilde{\mathcal{H}}\tilde{\mathcal{E}}^*\right] - \left(x_B^2 + (2 - x_B)^2\frac{t}{4M^2}\right)\mathcal{E}\mathcal{E}^* - x_B^2\frac{t}{4M^2}\tilde{\mathcal{E}}\tilde{\mathcal{E}}^*\Big\}. \quad (16)$$

The twist-3 term $\mathcal{C}^{DVCS}(\mathcal{F}^{\rm eff},\mathcal{F}^*)$ has an identical form, with one CFF factor replaced with the set $\mathcal{F}^{\rm eff}$. The $\mathcal{C}^{DVCS}(\mathcal{F}_T,\mathcal{F}^*)$, appearing with a $\cos(2\phi_{\gamma\gamma})$ weighting, also has the same form as Eq. (16), but now with one set $\mathcal{F}$ replaced by the set $\mathcal{F}_T$ of (twist-2) gluon transversity Compton form factors.

B. Bilinear DVCS term: E00-110 analysis and motivation for this proposal

The extremely rich harmonic structure of the DVCS cross section as a function of the azimuthal angle $\phi_{\gamma\gamma}$ provides an excellent tool to separate its different contributions. In E00-110 this technique allowed us to isolate the twist-3 contribution to the cross section, which turned out to be very small. However, even though the DVCS^2 terms in the cross section has a different $\phi_{\gamma\gamma}-$dependence than the interference terms (due to the absence of the BH propagators), the dependence is not sufficiently different to allow, in the present state, a reliable separation of these terms.

Let us summarize here the equations of the previous section, explain the approach adopted in E00-110 analysis, and motivate why we believe that the new experiment we propose herein is necessary in order to accurately understand the $ep \to ep\gamma$ reaction in terms of GPDs.

In summary, the DVCS helicity-independent ($d\sigma$) and helicity-dependent ($d\Sigma$) cross sections read:

$$\frac{d^5\sigma}{d^5\Phi} = \frac{1}{2}\left[\frac{d^5\sigma^+}{d^5\Phi} + \frac{d^5\sigma^-}{d^5\Phi}\right] = \frac{d^5\sigma(|BH|^2)}{d^5\Phi} + \Gamma_{DVCS}\,\mathcal{C}^{DVCS}(\mathcal{F},\mathcal{F}^*) + \frac{1}{\mathcal{P}_1(\phi_{\gamma\gamma})\mathcal{P}_2(\phi_{\gamma\gamma})}\Bigg(\{\Gamma_0^{\Re} - \cos(\phi_{\gamma\gamma})\Gamma_1^{\Re}\}\Re\mathrm{e}\left[\mathcal{C}^I(\mathcal{F})\right] + \Gamma_{0,\Delta}^{\Re}\Re\mathrm{e}\left[\mathcal{C}^I + \Delta\mathcal{C}^I\right](\mathcal{F}) + \cos(2\phi_{\gamma\gamma})\Gamma_2^{\Re}\Re\mathrm{e}\left[\mathcal{C}^I(\mathcal{F}^{\rm eff})\right]\Bigg), \quad (17)$$

$$\frac{d^5\Sigma}{d^5\Phi} = \frac{1}{2}\left[\frac{d^5\sigma^+}{d^5\Phi} - \frac{d^5\sigma^-}{d^5\Phi}\right] = \frac{1}{\mathcal{P}_1(\phi_{\gamma\gamma})\mathcal{P}_2(\phi_{\gamma\gamma})}\Bigg(\sin(\phi_{\gamma\gamma})\Gamma_1^{\Im}\Im\mathrm{m}\left[\mathcal{C}^I(\mathcal{F})\right] - \sin(2\phi_{\gamma\gamma})\Gamma_2^{\Im}\Im\mathrm{m}\left[\mathcal{C}^I(\mathcal{F}^{\rm eff})\right]\Bigg) + \sin(\phi_{\gamma\gamma})\Gamma_1^{\Im}\eta_{s1}\Im\mathrm{m}\left[\mathcal{C}^{\rm DVCS}(\mathcal{F}^{\rm eff},\mathcal{F}^*)\right] \quad (18)$$

where we only kept the leading (twist-2) contribution $\mathcal{C}^{DVCS}(\mathcal{F},\mathcal{F}^*)$ to the DVCS^2 term in the helicity-independent cross section. Only a twist-3 DVCS^2 contribution is present in the helicity-dependent cross section. We have also suppressed the mixing of the DVCS^2 term with the twist-3 $\sin(2\phi_{\gamma\gamma})$ and $\cos(2\phi_{\gamma\gamma})$ observables (see below Eqs. (22–23)). Note that the Γ_Λ factors in Eqs. (17) and (18) are functions of Q^2, x_B, t, and $s_e - M^2 = 2Mk$. They are explicitly independent of the azimuth $\phi_{\gamma\gamma}$.

In E00-110, due to the fact that we could not isolate the $\mathcal{C}^{DVCS}(\mathcal{F},\mathcal{F}^*)$ term (or $\mathcal{C}^{\rm DVCS}(\mathcal{F}^{\rm eff},\mathcal{F}^*)$) from its azimuthal dependence, we made an *effective* analysis, assuming

the DVCS^2 contribution to the cross section was negligible. This assumption implies that the *experimental* interference coefficients extracted actually contain a fraction of the neglected DVCS^2 contribution.

In each (x_B, Q^2) setting, for each bin in t, we therefore have the following experimental twist-2 DVCS observables:

$$\Im\mathrm{m}[\mathcal{C}^{\mathcal{I},\mathrm{exp}}(\mathcal{F})] = \Im\mathrm{m}[\mathcal{C}^{\mathcal{I}}(\mathcal{F})] + \langle\eta_{s1}\rangle\Im\mathrm{m}[\mathcal{C}^{DVCS}(\mathcal{F}^*,\mathcal{F}^{\mathrm{eff}})] \quad (19)$$

$$\Re\mathrm{e}\left\{[\mathcal{C}+\Delta\mathcal{C}]^{\mathcal{I},\mathrm{exp}}(\mathcal{F})\right\} = \Re\mathrm{e}\left\{[\mathcal{C}^{\mathcal{I}}+\Delta\mathcal{C}^{\mathcal{I}}](\mathcal{F})\right\} + \langle\eta_0\rangle\,\Re\mathrm{e}\left[\mathcal{C}^{\mathrm{DVCS}}(\mathcal{F}^*,\mathcal{F})\right] \quad (20)$$

$$\Re\mathrm{e}\left\{\mathcal{C}^{\mathcal{I},\mathrm{exp}}(\mathcal{F})\right\} = \Re\mathrm{e}\left\{\mathcal{C}^{\mathcal{I}}(\mathcal{F})\right\} + \langle\eta_{c1}\rangle\,\Re\mathrm{e}\left\{\mathcal{C}^{\mathrm{DVCS}}(\mathcal{F}^*,\mathcal{F})\right\}. \quad (21)$$

The coefficients $\langle\eta_\Lambda\rangle$ are the acceptance averaged ratios of the kinematic coefficients of the bilinear DVCS terms to the BH·DVCS terms. $\mathcal{C}^{\mathrm{DVCS}}(\mathcal{F},\mathcal{F}^*)$ is a twist-2 observable, as are the leading contributions of the BH·DVCS interference. In addition, we have the experimental twist-3 DVCS observables:

$$\Im\mathrm{m}[\mathcal{C}^{\mathcal{I},\mathrm{exp}}(\mathcal{F}^{\mathrm{eff}})] = \Im\mathrm{m}[\mathcal{C}^{\mathcal{I}}(\mathcal{F}^{\mathrm{eff}})] + \langle\eta_{s2}\rangle\Im\mathrm{m}[\mathcal{C}^{DVCS}(\mathcal{F}^*,\mathcal{F}^{\mathrm{eff}}))] \quad (22)$$

$$\Re\mathrm{e}[\mathcal{C}^{\mathcal{I},\mathrm{exp}}(\mathcal{F}^{\mathrm{eff}})] = \Re\mathrm{e}[\mathcal{C}^{\mathcal{I}}(\mathcal{F}^{\mathrm{eff}})] + \langle\eta_{c2}\rangle\Re\mathrm{e}[\mathcal{C}^{DVCS}(\mathcal{F}^*,\mathcal{F}^{\mathrm{eff}})]. \quad (23)$$

The values of the η_Λ coefficients in the E00-110 kinematics are summarized in Table I. They are small, though they grow with $|t|$. The bilinear term in Eq. (19) is a twist-3 observable, therefore the coefficient $\langle\eta_{s1}\rangle$ will decrease as $1/\sqrt{Q^2}$. We focus this proposal on separating the interference terms $C^{\mathcal{I}}(\mathcal{F})$ and $[C^{\mathcal{I}}+\Delta\mathcal{C}^{\mathcal{I}}](\mathcal{F})$ from the DVCS^2 term $\mathcal{C}^{\mathrm{DVCS}}(\mathcal{F},\mathcal{F}^*)$ in the helicity-independent cross section.

TABLE I: Weighting factors of bilinear DVCS terms for BH·DVCS observables in E00-110 at $Q^2 = 2.3$ GeV^2 and $x_B = 0.36$.

t (GeV^2)	-0.37	-0.33	-0.27	-0.23	-0.17
$\langle\eta_{s1}\rangle$	-0.0142	-0.0120	-0.0099	-0.0080	-0.0060
$\langle\eta_{s2}\rangle$	-0.048	-0.042	-0.036	-0.030	-0.023
$\langle\eta_{c1}\rangle$	-0.050	-0.048	-0.038	-0.033	-0.026
$\langle\eta_0\rangle$	+0.015	+0.024	+0.031	+0.039	+0.045
$\langle\eta_{c2}\rangle$	-0.038	-0.030	-0.022	-0.014	-0.010

C. Size of the DVCS bilinear term

Even though the coefficients $\langle \eta_\Lambda \rangle$ are small (less than 5% in E00-110, cf. Table I), the DVCS^2 GPD contribution $\mathcal{C}^{\rm DVCS}(\mathcal{F}, \mathcal{F}^*)$ is potentially large. We have several indications that the size of the DVCS^2 term $\mathcal{C}^{\rm DVCS}(\mathcal{F}, \mathcal{F}^*)$ can be important. Firstly, we have some experimental indications that come from the high precision data obtained in E00-110 itself. Secondly, theoretical models also predict this contribution to be large.

Fig. 2 shows (for one bin in Q^2 and t) the DVCS cross sections measured in E00-110 (top) and the experimental $\Re{\rm e}(C^I)$ and $\Re{\rm e}(C^I + \Delta C^I)$ extracted from its azimuthal analysis. The green curve in the unpolarized cross section $d^4\sigma$ (top plot, lower panel) shows the contribution of the BH to the cross section. The BH only accounts for half of the total cross section between 90° and 270°. It is unlikely that the DVCS^2 contribution is negligible, since the interference term (BH·DVCS) alone could not possibly account for the difference in this case.

Moreover, when looking at the lower plot in Fig. 2, we notice that the experimental coefficients $\Re{\rm e}(C^I)$ and $\Re{\rm e}(C^I + \Delta C^I)$ extracted are very different from each other. This is also very hard to explain if the DVCS^2 is small. Indeed, $\Re{\rm e}(\Delta C^I)$ is power-suppressed with respect to $\Re{\rm e}(C^I)$. The term $\Re{\rm e}(C^I + \Delta C^I)$ is expected to be close to $\Re{\rm e}(C^I)$, unless each has a distinct contribution from the neglected DVCS^2 term. Note from the values of η_0 and η_{c1} in Table I that the contribution of $\mathcal{C}^{DVCS}$ is approximately equal and opposite in our empirical $\Re{\rm e}(C^I)$ and $\Re{\rm e}(C^I + \Delta C^I)$ terms.

Finally, theoretical models support the large size of $\mathcal{C}^{\rm DVCS}(\mathcal{F}, \mathcal{F}^*)$. Fig. 3 shows the prediction for $\mathcal{C}^{\rm DVCS}(\mathcal{F}, \mathcal{F}^*)$ in a GPD model by Vanderhaeghen, Guichon and Guidal (VGG) [6–8]. In this model $\mathcal{C}^{\rm DVCS}(\mathcal{F}, \mathcal{F}^*) \sim 30$. Taking into account the acceptance averaged ratios of the kinematic coefficients of the bilinear DVCS terms to the BH·DVCS terms (∼5%), this implies a value of 1.5 to our experimental observables, which is of the same order of magnitude as these observables themselves (cf. Fig. 2). Thus, the contribution to the experimental extraction of GPD observables is important from theoretical calculations also.

Experimentally, we can determine $\mathcal{C}^{\rm DVCS}(\mathcal{F}, \mathcal{F}^*)$ if we make an accurate cross section measurement at constant x_B and t (and Q^2) at two different incident beam energies. This is possible thanks to the fact that the acceptance averaged ratios of the kinematic coefficients of the bilinear DVCS terms to the BH·DVCS, $\langle \eta_\Lambda \rangle$, depend on the beam energy, where as

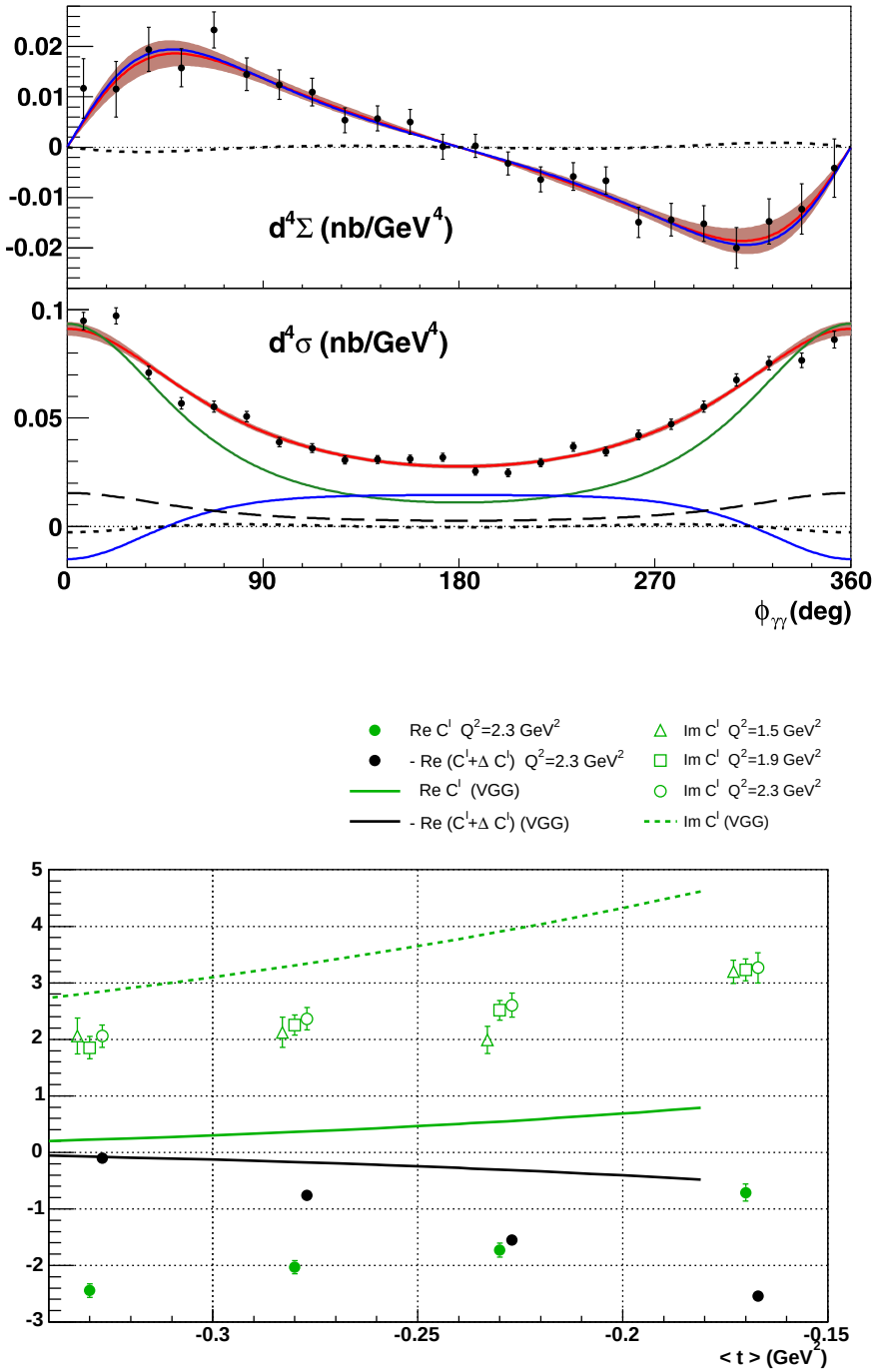

FIG. 2: Top: DVCS helicity-dependent ($d^4\Sigma$) and helicity-independent ($d^4\sigma$) cross sections measured in E00-110 for $Q^2 = 2.3$ GeV^2 and $\langle t \rangle = -0.28$ GeV^2. Bottom: Fourier analysis of the DVCS helicity-dependent (upper points) and unpolarized (lower points) DVCS cross section in E00-110 (PRL, in press [1]).

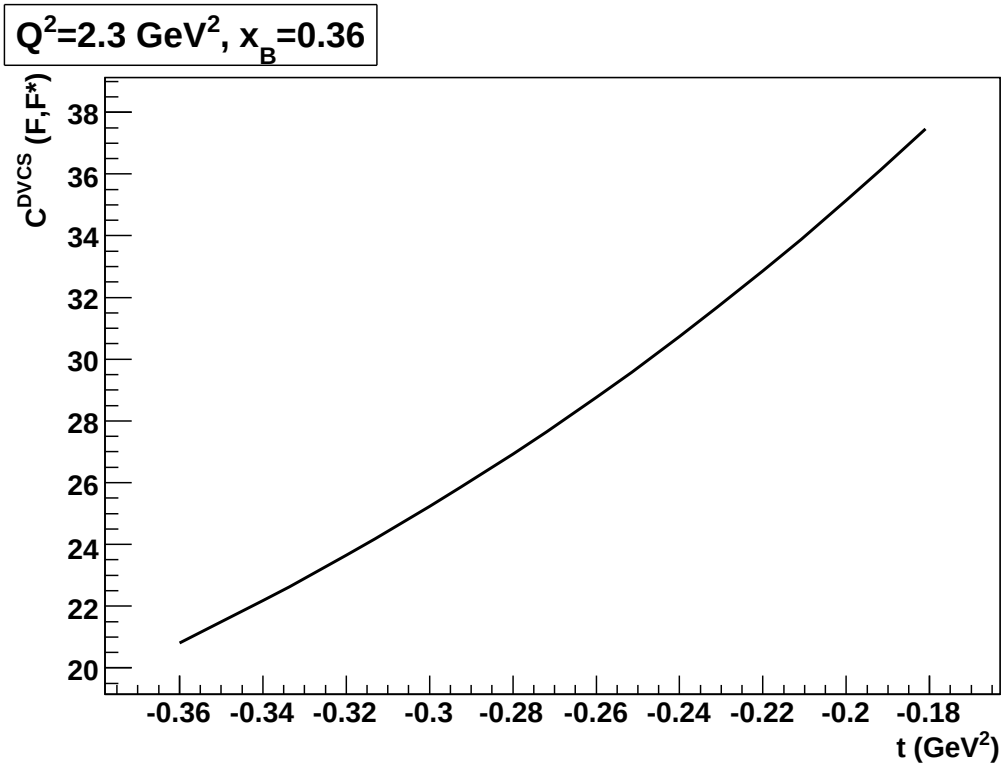

FIG. 3: VGG model estimate for $\mathcal{C}^{\rm DVCS}(\mathcal{F},\mathcal{F}^*)$.

the extracted coefficients ($\mathcal{C}^{\rm DVCS}(\mathcal{F},\mathcal{F}^*)$ and the interference counterparts) do not.

We believe that a measurement of $\mathcal{C}^{\rm DVCS}(\mathcal{F},\mathcal{F}^*)$ is essential in order to properly interpret the experimental DVCS observables in terms of GPDs. If $\mathcal{C}^{\rm DVCS}(\mathcal{F},\mathcal{F}^*)$ turns out to be important, as the elements above suggest, future measurements, the JLab 12 GeV program in particular, will need to adapt its experimental program in order to systematically separate the DVCS^2 from the interference contributions. This will require accurate cross section measurements at different beam energies as we propose in this experiment.

In summary, we request a total of three weeks of polarized beam. We will use 4 and 5 pass, or 3 and 5 pass beam at the present 6 GeV maximum beam energy at JLab. We will separate the $\Re{\rm e}[\mathcal{C}^I(\mathcal{F})]$, $\Re{\rm e}[\mathcal{C}^I+\Delta\mathcal{C}^I](\mathcal{F})$, and $\mathcal{C}^{DVCS}(\mathcal{F},\mathcal{F}^*)$ terms for $Q^2=1.5$, 1.9, and 2.3 GeV^2. These measurements will impact the comprehensive DVCS program with JLab at 12 GeV.

III. DEEP π^0 ELECTROPRODUCTION

The π^0 electroproduction longitudinal cross section provides an extremely interesting access to GPDs. Indeed, if the twist-2 contribution dominates the cross section, it provides a promising way to perform a flavor separation of GPDs. Moreover, π^0 production probes only the "polarized" GPDs in the nucleon ($\tilde{H}$ and $\tilde{E}$), which contain information about the spatial distribution of the quark spin. This complements DVCS measurements, where all GPDs participate.

At leading twist

$$\frac{d\sigma_L}{dt} = \frac{1}{2}\Gamma \sum_{h_N, h_{N'}} |\mathcal{M}^L(\lambda_M = 0, h'_N, h_N)|^2 \propto \frac{1}{Q^6} \qquad \frac{d\sigma_T}{dt} \propto \frac{1}{Q^8} \tag{24}$$

with

$$\mathcal{M}^L \propto \left[\int_0^1 dz \frac{\phi_\pi(z)}{z}\right] \int_{-1}^1 dx \left[\frac{1}{x-\xi} + \frac{1}{x+\xi}\right] \left\{\Gamma_1 \widetilde{H}_{\pi^0} + \Gamma_2 \widetilde{E}_{\pi^0}\right\}(x,\xi,t) \tag{25}$$

The Γ factors in Eq. (24) and Eq. (25) are kinematics factors and ϕ_π is the pion distribution amplitude. The flavor combination of GPDs entering in Eq. (25) is different from that in DVCS on the proton. Indeed,

$$|\pi^0\rangle = \frac{1}{\sqrt{2}}\{|u\bar{u}\rangle - |d\bar{d}\rangle\} \qquad \widetilde{H}_{\pi^0} = \frac{1}{\sqrt{2}}\left\{\frac{2}{3}\widetilde{H}^u + \frac{1}{3}\widetilde{H}^d\right\}, \tag{26}$$

whereas in DVCS on the proton:

$$|p\rangle = |uud\rangle \qquad H_{DVCS} = \frac{4}{9}H^u + \frac{1}{9}H^d\,. \tag{27}$$

As in the case of the DVCS unpolarized cross section, with these measurements we access a GPD integral over x. Note that at twist-2 level, the pion distribution amplitude $\phi_\pi(z)$ enters only as a normalization integral. Note also that the amplitude of Eq. (25) enters squared in the cross section. Therefore, a bilinear combination of these GPD integrals are measured.

The differential π^0 electroproduction cross section reads:

$$\frac{d\sigma}{dt} = \frac{d\sigma_T}{dt} + \epsilon\frac{d\sigma_L}{dt} + \sqrt{2\epsilon(1+\epsilon)}\frac{d\sigma_{LT}}{dt}\cos\phi + \epsilon\frac{d\sigma_{TT}}{dt}\cos 2\phi + \lambda\sqrt{2\epsilon(1-\epsilon)}\frac{d\sigma_{LT'}}{dt}\sin\phi \tag{28}$$

where λ electron helicity and where the virtual photon polarization is given by:

$$\epsilon = \left(1 + 2\frac{|\mathbf{q}|^2}{Q^2}\tan^2\frac{\theta}{2}\right)^{-1}. \tag{29}$$

E00-110 measured the π^0 electroproduction cross section at $Q^2 = 2.3$ GeV^2 and $E_b = 5.75$ GeV. From the azimuthal dependence of the total cross section, we were able to extract all 3 interference cross sections (σ_{LT}, σ_{TT} and $\sigma_{LT'}$) and the combination $\sigma_T + \epsilon\sigma_L$. Figs. 4–5 show the preliminary results of these cross section measurements.

In E00-110 we could not perform an L/T separation of the cross section in order to access the longitudinal part that is (potentially) related to GPDs. However, results shown in Fig. 5 provide indications that the longitudinal part of the cross section can be large. Indeed, all interference and transverse components prove to be very small compared to the contribution containing σ_L. Also, the VGG model predicts a sizable value for σ_L, and the meson exchange model from J.-M. Laget, which basically only includes transverse components, does not reproduce either the shape or the absolute values of our cross section data. Therefore, all these elements indicate that the longitudinal cross section may be large enough to allow an accurate determination.

We propose here to isolate the σ_L contribution for three different bins in Q^2, and therefore *measure all 5 independent cross sections* as a function of Q^2. We will be able to test for the first time the factorization of the longitudinal π^0 cross section and therefore demonstrate (or not) the feasibility of extracting GPD data from this interesting channel.

As in E00-110 (cf. Fig. 5), we will measure these cross sections as a function of t in the range $0.1 < -t < 0.4$ GeV^2. Another prediction of the hard reaction mechanism is that the t-dependence of the scattering amplitude originates solely from the GPD if the leading twist amplitude dominates. As a result, the $t-$slope of the cross section should become independent of Q^2 at fixed ξ.

Finally, note that the π^0 cross section is an essential element of our DVCS measurements but is not the main motivation of this proposal. An L/T separation experiment of the π^0 electroproduction cross section has already been approved by PAC30 for the 12 GeV program (PR12-06-108) in a larger kinematical domain. It will be interesting to see if the t-slope of π^0 electroproduction is different from the t-slope observed in DVCS. In terms of the impact parameter picture of the GPDs [9][10], these t-slopes need not be the same for H (which likely dominates the DVCS amplitude) as for $\tilde{H}$ and $\tilde{E}$, which enter the π^0 amplitude.

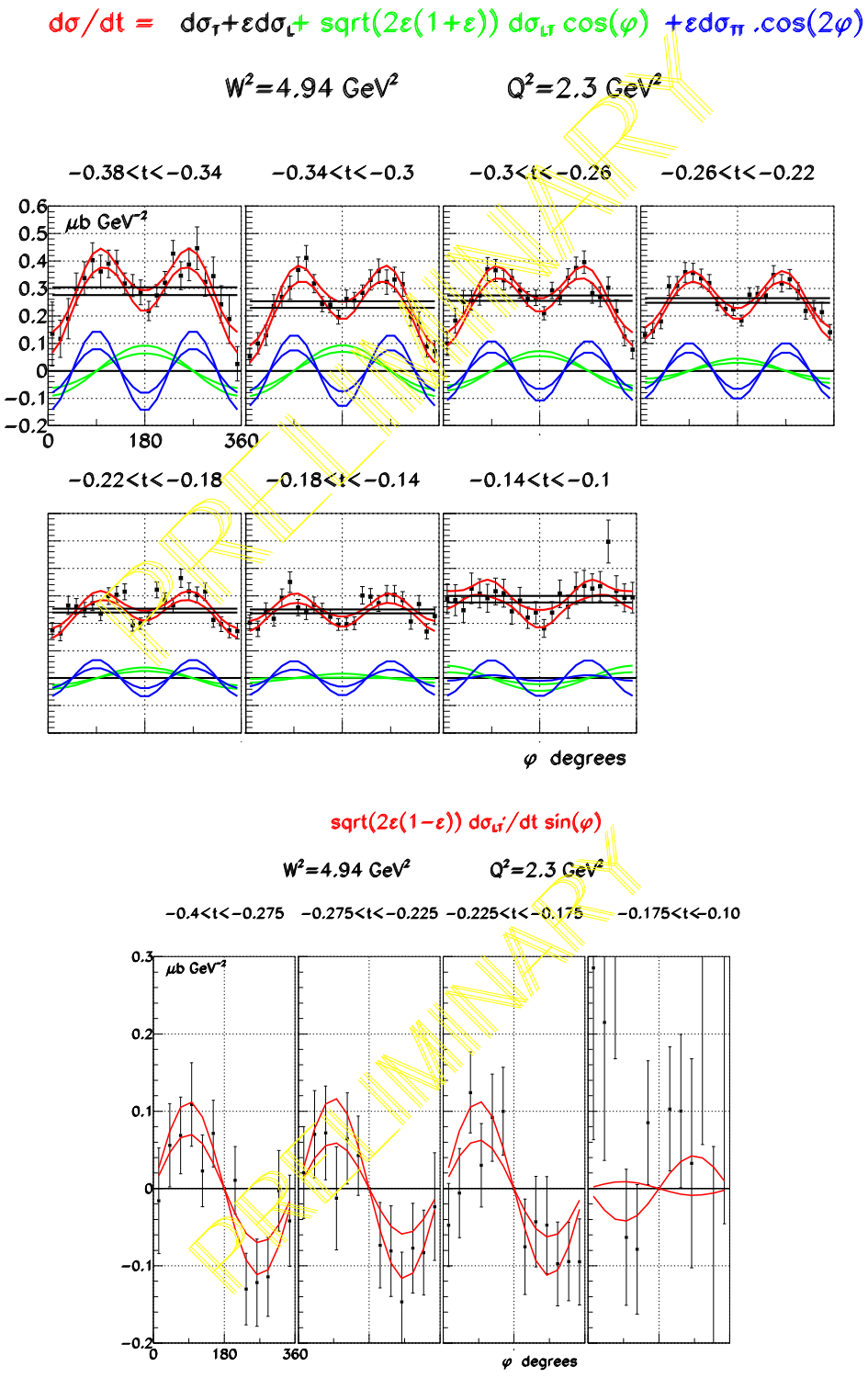

FIG. 4: π^0 electroproduction cross-section preliminary results from E00-110 ($Q^2 = 2.3$, $x_B = 0.36$) for each $t-$bin as a function of ϕ.

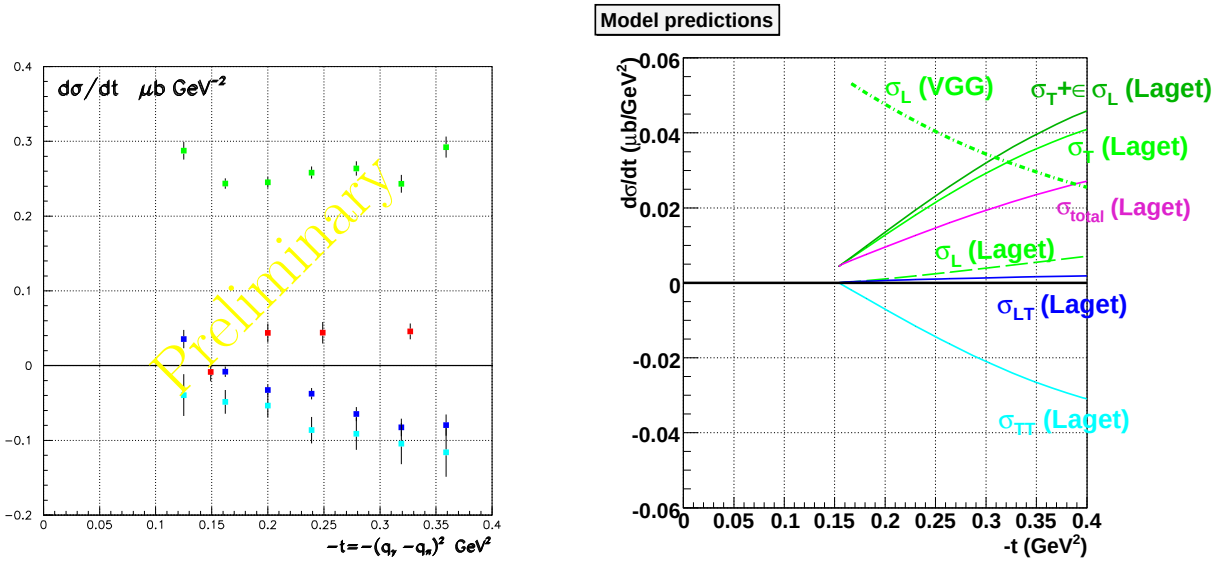

FIG. 5: π^0 electroproduction cross-section preliminary results from E00-110 ($Q^2 = 2.3$, $x_B = 0.36$). Green: $\frac{\sigma_T}{dt} + \epsilon\frac{\sigma_L}{dt}$, Light Blue: $\frac{\sigma_{LT}}{dt}$, Dark Blue: $\frac{\sigma_{TT}}{dt}$, and Red: $\frac{\sigma_{LT'}}{dt}$.

IV. EXPERIMENTAL SETUP AND ANALYSIS TECHNIQUE

This proposal is based directly on the experience of E00-110. The apparatus is the same as used during E00-110, with a 50% increase of the calorimeter size, as well as an upgrade of the calorimeter trigger. These upgrades will expand our acceptance in t and improve our π^0 reconstruction efficiency.

A. Experimental apparatus and calibration

We present a sketch of the DVCS layout in Hall A in Fig. 6. We use the standard 15 cm liquid hydrogen target. We detect the electrons in the HRS-L and photons (and $\pi^0 \to \gamma\gamma$) in a PbF_2 calorimeter at beam right. We note in Fig. 6 the modified scattering chamber from E00-110 and a new modified downstream beam pipe. The scattering chamber is 63 cm in radius, with a 1 cm Al spherical wall facing the PbF_2 calorimeter and a thin window (16 mil Al) facing the HRS-L.

We will detect the scattered photon in a 13×16 element PbF_2 calorimeter. This is the existing 11×12 E00-110 calorimeter, with 76 additional elements. Each block is 3×3 cm$^2 \times 20X_0$. The additional blocks will add two more rows on the top and bottom, and two

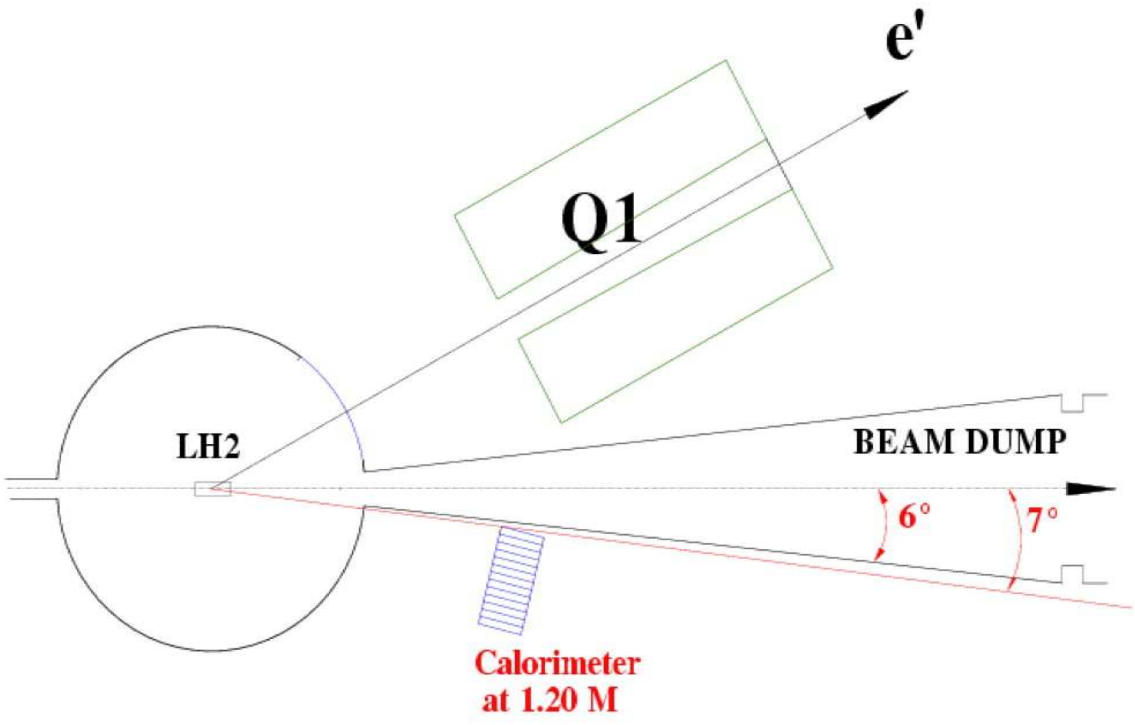

FIG. 6: Hall A DVCS experimental arrangement: the scattering chamber is identical to the E00-110 chamber, with a mid-plane 63 cm radius spherical section with 1 cm Al wall thickness, and a 16 mil Al window facing the HRS-L. We propose a conical downstream beam pipe, with half-opening angle of 6 degrees on beam-right, and length 3 m. The drawing shows the expanded PbF_2 calorimeter at beam-right, in the closest configuration: front face 120 cm from target center. The calorimeter is shown in its smallest angle setting (inner edge at 7°).

columns on the wide angle side. The properties of PbF_2 are summarized in Table II. The important design considerations for DVCS are as follows:

- PbF_2 is a radiation hard pure Cerenkov crystal medium [11];
- With no scintillation light [12], the calorimeter signal is insensitive to low energy hadrons, and the pulse rise and fall time is determined only by geometry and the response of the PMT. This allows us to use the 1GHz Analog Ring Sampler (ARS) digitizer [13] to minimize pileup (see section IV B for more details).
- The high luminosity of this proposal requires fast response PMTs operated at low gain and capacitively coupled to a pre-amplifier. The low gain reduces the DC anode

current. The capacitive coupling removes the average pile-up from low energy γ-rays.

- The small Molière radius (2.2 cm) allows us to separate closely spaced showers from π^0 decay, and minimize shower leakage at the boundary.

- The short radiation length minimizes fluctuations in light collection from fluctuations in the longitudinal profile of the shower.

- The low value 9 MeV of the critical energy (roughly the energy threshold for which bremsstrahlung energy loss exceeds ionization loss for electrons) also improves the resolution *e.g.* relative to Pb-Glass.

- In E00-110, we obtained a signal of 1 photo-electron per MeV of deposited energy in the E.M. shower, and an energy resolution of 2.4% from elastic H$(e, e'_{Calo} p_{HRS})$ electron of 4.2 GeV. For our simulations, we project a resolution of $\sigma_E/E = 2.0\% \oplus (3.2\%)\sqrt{(1\,\mathrm{GeV})/q'}$. We also achieved a spatial resolution of 2 mm at 4.2 GeV. From the combination of energy and spatial resolution, we obtained a $\pi^0 \to \gamma\gamma$ mass resolution of 9 MeV.

TABLE II: Properties of PbF_2.

Density		7.77 g/cm^3
Radiation Length		0.93 cm
Molière Radius		2.20 cm
Index of Refraction	($\lambda = 180$ nm)	2.05
	($\lambda = 400$ nm)	1.82
Critical Energy		9.04 MeV

We will calibrate the calorimeter via elastic H$(e, e'_{Calo} p_{HRS})$ measurements. Three sequences of calibration will be performed : one day each at the beginning, middle, and end of each scheduled period of running time. We will then cross calibrate all of the blocks and maintain a continuous monitoring of the calibration using the π^0 mass reconstruction from H$(e, e'\pi^0)X$ events. The elastic calibration will also be used to verify the geometrical surveys of the spectrometer and calorimeter.

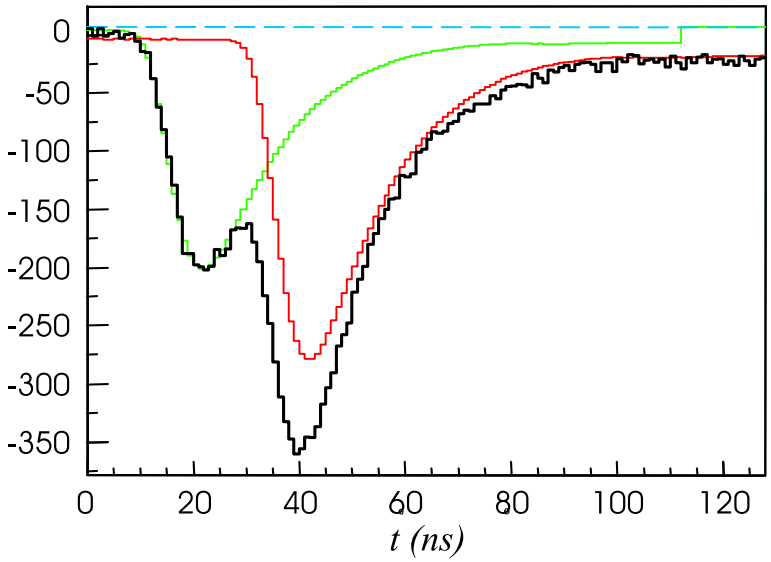

FIG. 7: PMT signals are recorded in a 128 ns window at a sampling rate of 1 GHz. The offline treatment of these data allows to resolve pile-up events, as the one shown in this figure. In E00-110, the blocks closest to the beam had a maximum 20% double pulse probability.

B. The ARS sampling system

The same acquisition system used with the E00-110 calorimeter will be used. It is based on the Analog Ring Sampler (ARS) [13]. It consists of an array of 128 capacitor cells, which continuously sample the PMT signal at a rate of 1 GHz. When a trigger is received (by the HRS), the sampling is stopped and the charge of each capacitor is proportional to the value of the PMT signal. If the event is a good photon candidate (see section IV C for details on the calorimeter trigger), the charge on each of the capacitors is digitized using flash-ADCs and the information transfered to the data stream.

Fig. 7 shows a typical recorded signal. The digitization provided by the ARS system allows to treat the signal offline to resolve pile-up events as the one shown in Fig. 7.

The limiting factor for the luminosity of the Hall A DVCS experiments is the pile-up rate in the ARS analysis window. This window was chosen to be 20 ns around the coincidence time, which is the typical width of the PbF_2 signal. For each kinematical setting we propose to run at the maximum instantaneous luminosity that we were successful to cope with during E00-110 and E03-106 [22]. However, as we propose to run the whole experiment at

this maximum luminosity, we plan to carry out some performance tests of the optical curing procedure during the summer 2007 (see details in Appendix A). This (shorter) experiment we propose herein will fully validate the feasibility of our approved (longer) 12 GeV DVCS program (PR12-06-114) [14], which relies on the successful optical curing of the calorimeter radiation damage. We will need a total of three curing cycles during this experiment, each taking 1 day of time. Therefore, three additional days are to be added for this purpose to our actual beam time used.

C. Upgraded calorimeter trigger

Experiment E00-110 was focused on the exclusive DVCS process in the three kinematic settings of Table III. The table also indicates the range in energies of the exclusive DVCS photons, corresponding to the HRS acceptance and the geometrical acceptance of the calorimeter. The experimental trigger consisted of a standard electron trigger in the HRS, validated by the photon calorimeter. The calorimeter validation is based on a fast integration/digitization of all blocks following the electron trigger, with parallel logic constructing the digital sum of all overlapping sets of 4 contiguous blocks (square pattern). Each set of four is a "tower". The event validation required at least one tower above a threshold value Th_{tower}. Only if this condition was achieved were all ARS channels digitized and readout to the event stream. The nominal threshold of 1 GeV for the trigger has a dispersion due to the mis-calibration of each block ($\sim$ 100 MeV) and each ADC channel (100 MeV) in addition to the intrinsic energy resolution of the calorimeter (40 MeV at 1 GeV) which must be added. All of this sets an effective threshold of $Th_{tower} \approx 1.1$ GeV. Table III shows the minimum, nominal and maximum energies of the real DVCS photon, showing that the threshold allowed a 100% detection efficiency of exclusive DVCS photons.

The threshold, $Th_{tower} = 1$ GeV, set on the towers (any of 4 contiguous blocks) was low enough to ensure 100% detection efficiency of exclusive DVCS photons. In addition, this threshold allows us to record and study inclusive DVCS events $\mathrm{H}(e, e'\gamma)X$ for the range of inelasticity (M_X^2) determined by

$$q'_{\mathrm{inel}} \approx \frac{W^2 - M_X^2}{2M(1-x_B)} > Th_{tower}. \tag{30}$$

For each $H(e,e'\gamma)X$ event, we define the inelasticity as

$$q'(\text{exclusive}) - q' \;=\; \frac{M_X^2 - M^2}{2M(1-x_B)}\,. \tag{31}$$

In principle, our calorimeter threshold allows us to study the photon electroproduction process with an inelasticity up to $q'_{min} - Th_{tower}$. However, to obtain a pure DVCS sample, it is mandatory to subtract the events where the single detected photon comes from the decay of a π^0. We perform this subtraction as explained in [1] using the detected $H(e,e'\pi^0)X$ events. Based on our trigger, π^0 events were recorded only if **both** of the two photons of the decay were above the calorimeter tower threshold Th_{tower}. This subtraction depends of course on the π^0 statistics, and the more the better. With a threshold Th_{tower} we could detect the π^0 and perform the subtraction only if $E_\pi \approx q' > 2Th_{tower}$ and the probability to detect π^0 is then $1 - 2(Th_{tower})/q'$. Thus the value $Th_{tower} = 1.1$ GeV and our trigger scheme limited the possibility π^0 subtraction to an in-elasticity of 0.0, 0.1 and 0.6 GeV for the kinematics 1, 2 and 3 respectively. This was enough for kinematic 3, but for the kinematics 2 and 1, our π^0 sample was only sufficient for the extraction of the helicity-correlated cross sections, and not the helicity-independent cross sections [23]. Nor were we able to obtain $H(e,e'\pi^0)p$ cross sections in kinematics 1 and 2.

To overcome this inefficiency and detect low energy π^0, we will replace the trigger over tower Th_{tower} by a trigger on the total energy deposit in the calorimeter Th_Σ and then we will record all the blocks (or perhaps if necessary to decrease the dead time, the blocks of the tower above a very low threshold of 0.3 GeV for instance).

Kinematic	Q^2	Min q'	Nominal q'	Max q'
	GeV^2	GeV	GeV	GeV
I	1.5	1.6	2.1	2.5
II	1.9	2.3	2.7	3.1
III	2.3	2.8	3.3	3.8

TABLE III: Kinematic settings of E00-110, including the minimum, nominal and maximum photon energy in the calorimeter for exclusive $H(e,e'\gamma)p$ events.

Kinematic	Q^2 GeV^2	minimum INELAS. GeV	nominal INELAS. GeV	Maximum INELAS. GeV
I	1.5	0.0	0.0	0.2
II	1.9	0.1	0.5	0.9
III	2.3	0.6	1.1	1.6

TABLE IV: E00-110 Allowed theoretical inelasticity (INELAS) for reconstruction of $\pi^0 \rightarrow \gamma\gamma$ events, with a threshold of 1.1 GeV on each of two towers

Kinematic	Q^2 GeV^2	Th_Σ GeV	minimum INELAS. GeV
I	1.5	1.2	0.4
II	1.9	1.7	0.6
III	2.3	2.0	0.8

TABLE V: Allowed minimum inelasticity with threshold Th_Σ on the total energy deposit in the calorimeter (new proposal).

D. Exclusivity of the DVCS reaction

The exclusivity of the DVCS reaction will be based on the missing mass technique, successfully used during E00-110. Fig. 8 presents the missing mass squared obtained in E00-110 for H$(e, e'\gamma)X$ events, with coincident electron-photon detection. After subtraction of an accidental coincidence sample, our data is essentially background free: we have negligible contamination of non-electromagnetic events in the HRS and PbF_2 spectra. In addition to H$(e, e'\gamma)p$, however, we do have the following competing channels: $ep \rightarrow e\pi^0 p$, $ep \rightarrow e\pi^0 N\pi$, $ep \rightarrow e\gamma N\pi$, $ep \rightarrow e\gamma N\pi\pi \ldots$. From symmetric (lab-frame) π^0-decay, we obtain a high statistics sample of H$(e, e'\pi^0)X'$ events, with two photon clusters in the PbF_2 calorimeter. From these events, we determine the statistical sample of [asymmetric] H$(e, e'\gamma)\gamma X'$ events that must be present in our H$(e, e'\gamma)X$ data. The M_X^2 spectrum displayed in black in Fig. 8 was obtained after subtracting this π^0 yield from the total (green) distribution. This is a 14% average subtraction in the exclusive window defined by 'M_X^2 cut' in Fig. 8. Depending on the bin in $\phi_{\gamma\gamma}$ and t, this subtraction varies from 6% to 29%. After our π^0 subtraction,

the only remaining channels, of type H$(e,e'\gamma)N\pi$, $N\pi\pi$, *etc.* are kinematically constrained to $M_X^2 > (M+m_\pi)^2$. This is the value ('M_X^2 cut' in Fig. 8) we chose for truncating our integration. Resolution effects can cause the inclusive channels to contribute below this cut. To evaluate this possible contamination, during E00-110 we used an additional proton array (PA) of 100 plastic scintillators. The PA subtended a solid angle (relative to the nominal direction of the **q**-vector) of $18^\circ < \theta_{\gamma p} < 38^\circ$ and $45^\circ < \phi_{\gamma p} = 180^\circ - \phi_{\gamma\gamma} < 315^\circ$, arranged in 5 rings of 20 detectors. For H$(e,e'\gamma)X$ events near the exclusive region, we can predict which block in the PA should have a signal from a proton from an exclusive H$(e,e'\gamma p)$ event. The red histogram is the $X=(p+y)$ missing mass squared distribution for H$(e,e'\gamma p)y$ events in the predicted PA block, with a signal above an effective threshold 30 MeV (electron equivalent). The blue curve shows our inclusive yield, obtained by subtracting the normalized triple coincidence yield from the H$(e,e'\gamma)X$ yield. The (smooth) violet curve shows our simulated H$(e,e'\gamma)p$ spectrum, including radiative and resolution effects, normalized to fit the data for $M_X^2 \leq M^2$. The cyan curve is the estimated inclusive yield obtained by subtracting the simulation from the data. The blue and cyan curves are in good agreement, and show that our exclusive yield has less than 2% contamination from inclusive processes. In this new experiment, the kinematics being the same as in E00-110, the missing mass resolution will remain the same. We will apply the same technique to ensure exclusivity: apply a tight cut on the missing mass distribution in order to eliminate all inclusive channels. The systematic uncertainty will remain of the same order as in E00-110 (around 2%). *We will not need to detect the recoil proton in this new experiment.*

E. Analysis technique

Let us describe briefly here the analysis technique we used in E00-110. The same technique with the supplementary term $\mathcal{C}^{DVCS}(\mathcal{F},\mathcal{F}^*)$ will be simulated in order to extract the projected results of this proposal (cf. section VI A). Once again, the DVCS (helicity-

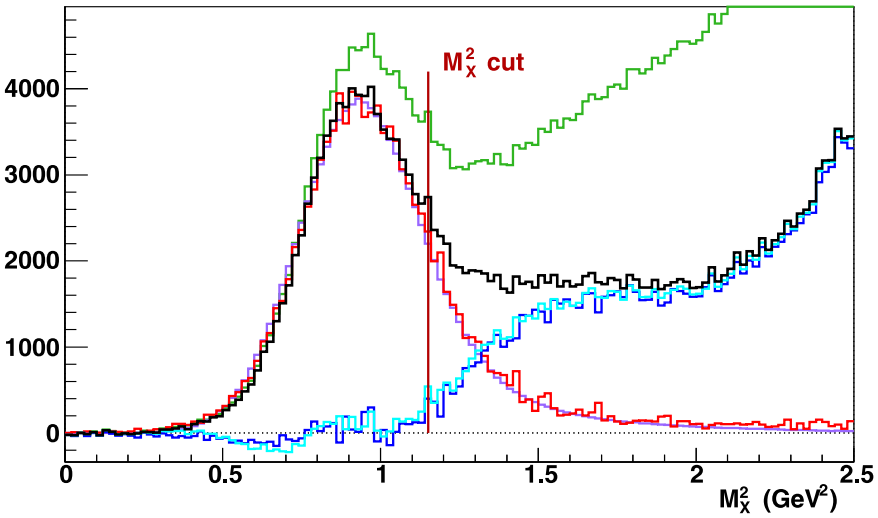

FIG. 8: Missing mass squared in E00-110 for H$(e,e'\gamma)X$ events (green curve) at $Q^2 = 2.3$ GeV^2 and $-t \in [0.12, 0.4]$ GeV^2, integrated over the azimuthal angle of the photon $\phi_{\gamma\gamma}$. The black curve shows the data once the H$(e,e'\gamma)\gamma X'$ events have been subtracted. The other curves are described in the text.

independent) cross section reads:

$$\frac{d^5\sigma}{d^5\Phi} = \frac{1}{2}\left[\frac{d^5\sigma^+}{d^5\Phi} + \frac{d^5\sigma^-}{d^5\Phi}\right] = \frac{d^5\sigma(|BH|^2)}{d^5\Phi} + \frac{d^5\sigma(|DVCS|^2)}{d^5\Phi} + \frac{1}{\mathcal{P}_1(\phi_{\gamma\gamma})\mathcal{P}_2(\phi_{\gamma\gamma})}\times$$
$$\left(\{\Gamma_0^{\Re} - \cos(\phi_{\gamma\gamma})\Gamma_1^{\Re}\}\Re\mathrm{e}\left[\mathcal{C}^I(\mathcal{F})\right] + \Gamma_{0,\Delta}^{\Re}\Re\mathrm{e}\left[\mathcal{C}^I + \Delta\mathcal{C}^I\right](\mathcal{F}) + \cos(2\phi_{\gamma\gamma})\Gamma_2^{\Re}\Re\mathrm{e}\left[\mathcal{C}^I(\mathcal{F}^{\mathrm{eff}})\right]\right), \tag{32}$$

where the term $d^5\sigma(|DVCS|^2)/d^5\Phi$ was neglected in the E00-110 analysis.

In our simulation, we generate events uniformly in a fixed electron phase space $\Delta^3\Phi_e = \Delta Q^2 \Delta x_B \Delta\phi_e$ and in a photon phase space $\Delta^2\Phi_\gamma = 2\pi[t_{\min}(Q^2, x_B) - t_{\max}]$. The bound $t_{\max} = -1$ GeV^2 is an arbitrarily fixed upper bound, and $t_{\min} \approx -x_B^2 M^2/[1 - x_B]$ is the event-by-event kinematic upper bound on $t < 0$. We simulate internal bremsstrahlung in the scattering process and external bremsstrahlung and ionization straggling in the target and scattering chamber windows. We include spectrometer resolution and acceptance effects and a full GEANT3 simulation of the detector response to the DVCS photons and protons. The spectrometer acceptance is defined for both the data and simulation by a R-function cut [15]. Radiative corrections for virtual photons and unresolved real photons are applied according to the VCS (BH+Born amplitude) specific prescriptions of Ref. [16]. This results

in a global correction factor (independent of $\phi_{\gamma\gamma}$ or helicity) of 0.91 ± 0.02 applied to our experimental yields. Within the quoted uncertainty, this correction is independent of the kinematic setting.

For each (Q^2, x_B, t) bin, we fit the $\Re$e parts of the harmonics $\mathcal{C}_\Gamma \in \{\mathcal{C}^{\mathcal{I}}(\mathcal{F}), \mathcal{C}^{\mathcal{I}}(\mathcal{F}^{\rm eff}), \left[\mathcal{C}^{\mathcal{I}} + \Delta\mathcal{C}^{\mathcal{I}}\right](\mathcal{F})\}$ as independent parameters. We minimize:

$$\chi^2 \;=\; \sum_i \left[\left(Y_i^{\rm Exp} - Y_i^{\rm Fit} \right)^2 / \sigma_i^2 \right]. \tag{33}$$

The $Y_i^{\rm Exp}$ are the experimental yields, after accidental and π^0 subtractions, in bin i, with statistical errors σ_i. The fit yields, $Y_i^{\rm Fit} = \sum_\Gamma \mathcal{C}_\Gamma K_\Gamma(i)$, depend linearly on the fitting harmonics $\mathcal{C}_\Gamma$ and the Monte-Carlo integrated kinematic weights:

$$K_\Gamma(i) \;=\; \mathcal{L} \sum_{j=1}^{N^{\rm sim}} \frac{\Delta^3\Phi_e \Delta^2\Phi_\gamma(j)}{N^{\rm sim}} \Gamma_\Gamma(j) \eta(i,j). \tag{34}$$

$\mathcal{L}$ is the integrated experimental luminosity and $N^{\rm sim}$ is the total number of events in the simulation. The indicator function $\eta(i,j) = 1$ if simulation event j lands in experimental bin i, otherwise, $\eta(i,j) = 0$. After fitting the harmonics $\mathcal{C}_\Gamma$ to our experimental yields, we extract the experimental cross section (and associated error bars)

$$\frac{d^5\sigma^{\rm Exp}(i)}{d^5\Phi} \;=\; \frac{d^5\sigma^{\rm Fit}(i)}{d^5\Phi} Y_i^{\rm Exp} / Y_i^{\rm Fit}, \tag{35}$$

where $d^5\sigma^{\rm Fit}$ is defined by our fitted parameters and Eq. (32).

V. PROPOSED KINEMATICS AND BEAM TIME REQUEST

Table VI summarizes our proposed kinematics and beam time request. For each Q^2 setting, we propose two different energies to allow both the DVCS^2 separation from the BH·DVCS interference terms, and the conventional Rosenbluth separation of $d\sigma_L$ and $d\sigma_T$ in the exclusive deep virtual π^0 channel. The integrated luminosity or beam time for the higher beam energy setting ($E_b = 6$ GeV) has been computed in order to achieve the same statistical uncertainty as our systematics (see section VI A for a discussion of the systematics uncertainties). This is the same integrated luminosity we achieved in E00-110, where similar kinematic settings were used.

At each Q^2 point, for the low energy point we are requesting three times the integrated luminosity as at the 6 GeV beam setting. This is a consequence of the behavior of the cross

sections for both the DVCS and π^0 channels. The deeply virtual exclusive π^0 electroproduction counting rates are essentially proportional to the DIS cross section. These cross sections fall by roughly a factor of 3 as we lower the beam energy at fixed Q^2 (a factor of 4 at the $Q^2 = 1.5$ GeV^2 setting). Therefore we request the higher integrated luminosity at low energy to match the statistical and systematic errors of the two beam settings. We present the DVCS cross sections in detail in section VI A. At fixed Q^2, the count rate *rises* as we lower the beam energy, but this is because of the increase of the BH amplitude. Thus the relative contribution of the DVCS^2 and BH·DVCS interference terms decreases as we lower the beam energy. In order to maintain the same net statistical contribution to the DVCS separations from the two beam energy settings, we must increase the beam time at the lower energy setting. These considerations determined our beam request in Table VI. The full impact of our statistical and systematic errors on our projected results is presented in the next section.

Three additional days are needed for three elastic calibrations of the calorimeter and three more days (total) for the optical curing of its radiation damage.

VI. PROJECTED RESULTS

A. Bilinear DVCS separation

In order to estimate the accuracy on the extraction of the DVCS^2 (and the interference) terms, we have simulated the extraction procedure used in E00-110 and described in section IV E.

Firstly, using our simulation of the experimental apparatus, we computed the Monte-Carlo integrated kinematic weights of Eq. (34). In this new experiment, we have an additional $K_\Gamma(i)$ and an additional $\mathcal{C}_\Gamma$ associated with $\mathcal{C}^{DVCS}(\mathcal{F}, \mathcal{F}^*)$. Each experimental bin in E00-110 is now divided into 2 bins, each corresponding to one different beam energy. Secondly, we calculated the expected number of counts in each bin as:

$$Y_i^{Exp} = \mathcal{L} \sum_\Gamma K_\Gamma(i) \eta(i,j) \cdot \mathcal{C}_\Gamma \tag{36}$$

To do that, we used a value of $\mathcal{C}^{DVCS}(\mathcal{F}, \mathcal{F}^*) = 20$ (independent of t). This is the smallest value predicted by the VGG model in our t range, and thus will give us the most pessimistic

	KIN I		KIN II		KIN III	
Q^2 (GeV^2)	1.5		1.9		2.3	
x_B	0.36		0.36		0.36	
W^2 (GeV^2)	3.78		4.26		4.96	
q' (GeV)	2.14		2.73		3.32	
k (GeV)	6.00	3.64	6.00	4.82	6.00	4.82
ϵ	0.873	0.566	0.792	0.652	0.683	0.473
k' (GeV)	3.78	1.42	3.19	2.01	2.59	1.41
θ_e (deg)	14.77	31.26	18.13	25.60	22.16	32.22
θ_q (deg)	-22.3	-16.89	-18.45	-16.07	-15.22	-12.18
θ_{Calo} (deg)	-22.3	-16.89	-18.45	-16.23	-16.23	-16.23
$\Gamma\Delta k'$	5.29 10^{-4}	3.86 10^{-5}	2.28 10^{-4}	6.74 10^{-5}	9.94 10^{-5}	2.20 10^{-5}
$d\sigma_{DIS}$ (nb)	69.1	12.5	26.2	11.9	11.0	4.32
Beam time (h)	**20**	**60**	**30**	**90**	**50**	**150**
Total beam time requested : 400 h + 72 h (calib.) + 72 h (calo. curing) = **544 h**						

TABLE VI: Proposed kinematics and beam time request. The nominal direction of the virtual photon $q = k - k'$ is θ_q. It corresponds to the angle of the calorimeter center θ_{Calo} whenever this is allowed by the mechanical constraints. In the $Q^2 = 2.3$ GeV^2 settings, the calorimeter edge closest to the beam is at the minimum angle of 7 degrees, and θ_{Calo} differs from θ_q. The virtual photon flux multiplied by the HRS momentum acceptance is $\Gamma\Delta k'$.

estimate in the relative uncertainty of the measurement. As far as the interference coefficients $\mathcal{C}_\Gamma$ are concerned, we used the values we obtained in E00-110 at $Q^2 = 2.3$ GeV^2 when we assumed $\mathcal{C}^{DVCS}(\mathcal{F}, \mathcal{F}^*) = 20$ (instead of assuming $\mathcal{C}^{DVCS}(\mathcal{F}, \mathcal{F}^*) = 0$, as in our previous analysis). The associated statistical uncertainties of Y_i^{Exp} are simply $\sigma(Y_i^{Exp}) = \sqrt{Y_i^{Exp}}$.

With the (simulated) experimental counts per bin Y_i^{Exp}, their statistical uncertainties $\sigma(Y_i^{Exp})$, and the kinematic weights $K_\Gamma(i)$, we applied exactly the same procedure described in section IV E, and used in E00-110.

In Fig. 8–10, we show the projected cross sections and extracted GPD terms for each of

Type		Relative errors (%)	
		E00-110	proposed
Luminosity	target length and beam charge	1	1
HRS-Calorimeter	Drift chamber multi-tracks	1.5	1.5
	Acceptance	2	2
	Trigger dead-time	0.1	0.1
DVCS selection	π^0 subtraction	3	1
	e(p,e'γ)πN contamination	2	2
	radiative corrections	2	2
Total cross section sum		4.9	4.0

TABLE VII: Relative systematic error budget for E00-110 and for the proposed experiment.

our three Q^2 points. The top two rows of each figure show the projected differential cross sections, at the two chose beam energies. The next two rows show the differential cross sections after subtracting the pure BH term. This residual is fitted by adjusting just the amplitude of each GPD term, since the $\phi_{\gamma\gamma}$-dependence of each term is defined by theory. The fits are done independently in each t-bin, but simultaneously at the two beam energies. According to our beam time request, we assumed the same statistical accuracy on the cross section determination as in E00-110 for the $E_b = 6$ GeV setting, and 3 times the E00-110 luminosity for the low E_b setting for each Q^2. The statistical (error bars) and systematic (green boxes) uncertainties in each extracted coefficient are shown in the bottom plots.

Table VII shows the systematic uncertainties of E00-110 and those of this proposal. Thanks to the trigger upgrade we will be able to detect a high statistics sample of π^0 events and the uncertainty in the subtraction from DVCS events will reduce the total systematics from 4.9% to 4.0%.

In order to estimate how our 4% systematic uncertainty in the cross section measurements propagates to the extracted interference and DVCS^2 coefficients, we performed the same procedure described above but with a number of counts Y_i^{Exp} (Eq. 36) 4% larger (or smaller). The difference obtained in the extracted coefficients is plotted as the systematic error (green boxes) in the bottom plots of Figs. 9–11.

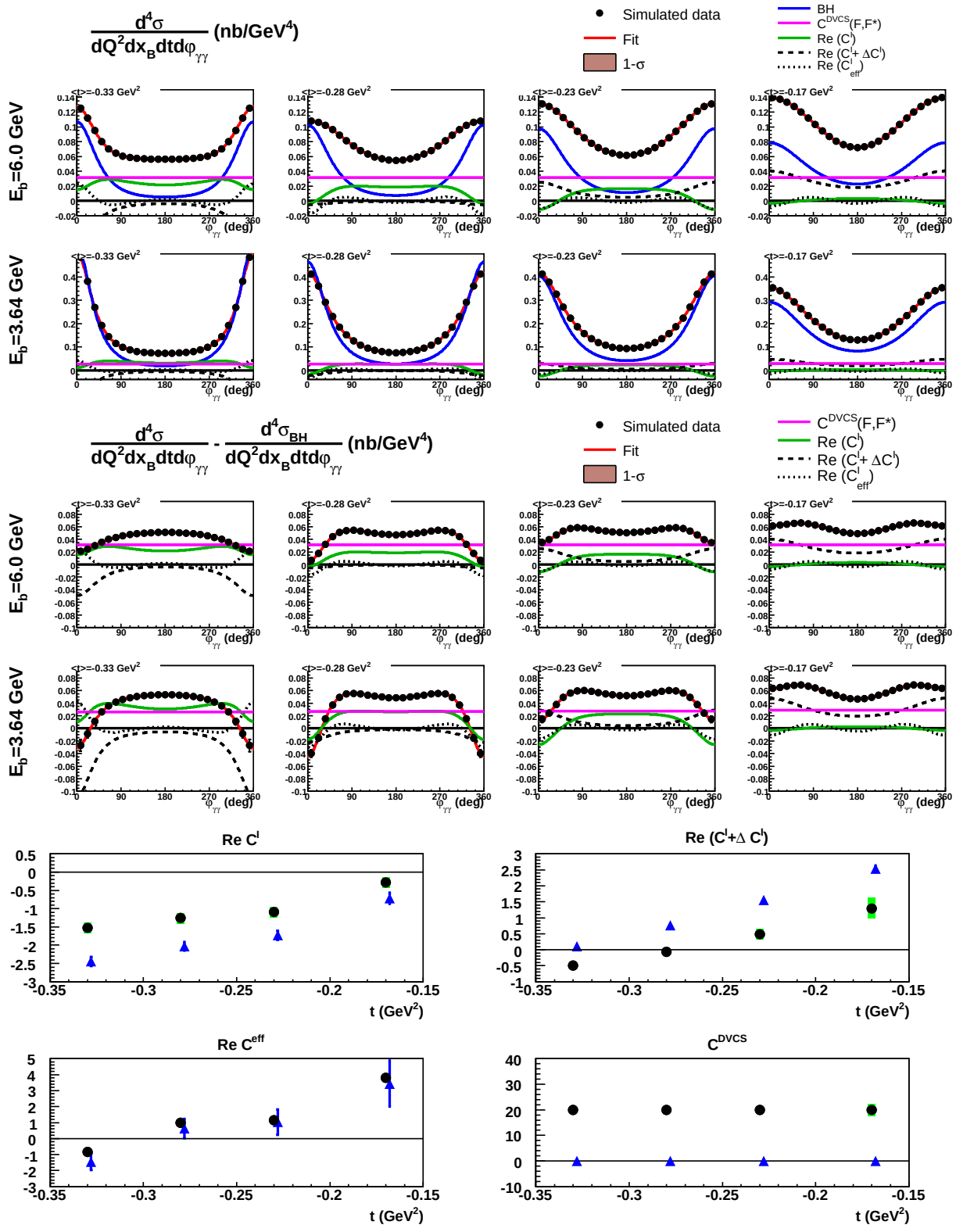

FIG. 9: Projected cross-section measurements for the $Q^2 = 1.5$ GeV^2 setting. $\mathcal{C}^{\rm DVCS}(\mathcal{F},\mathcal{F}^*) = 20$ in this estimate. Bottom plots show the statistical (error bars) and the systematic (green boxes) uncertainties in each of the extracted (interference and DVCS^2) coefficients (black dots), compared to E00-110 extraction (blue triangles, slightly offset for visual clarity).

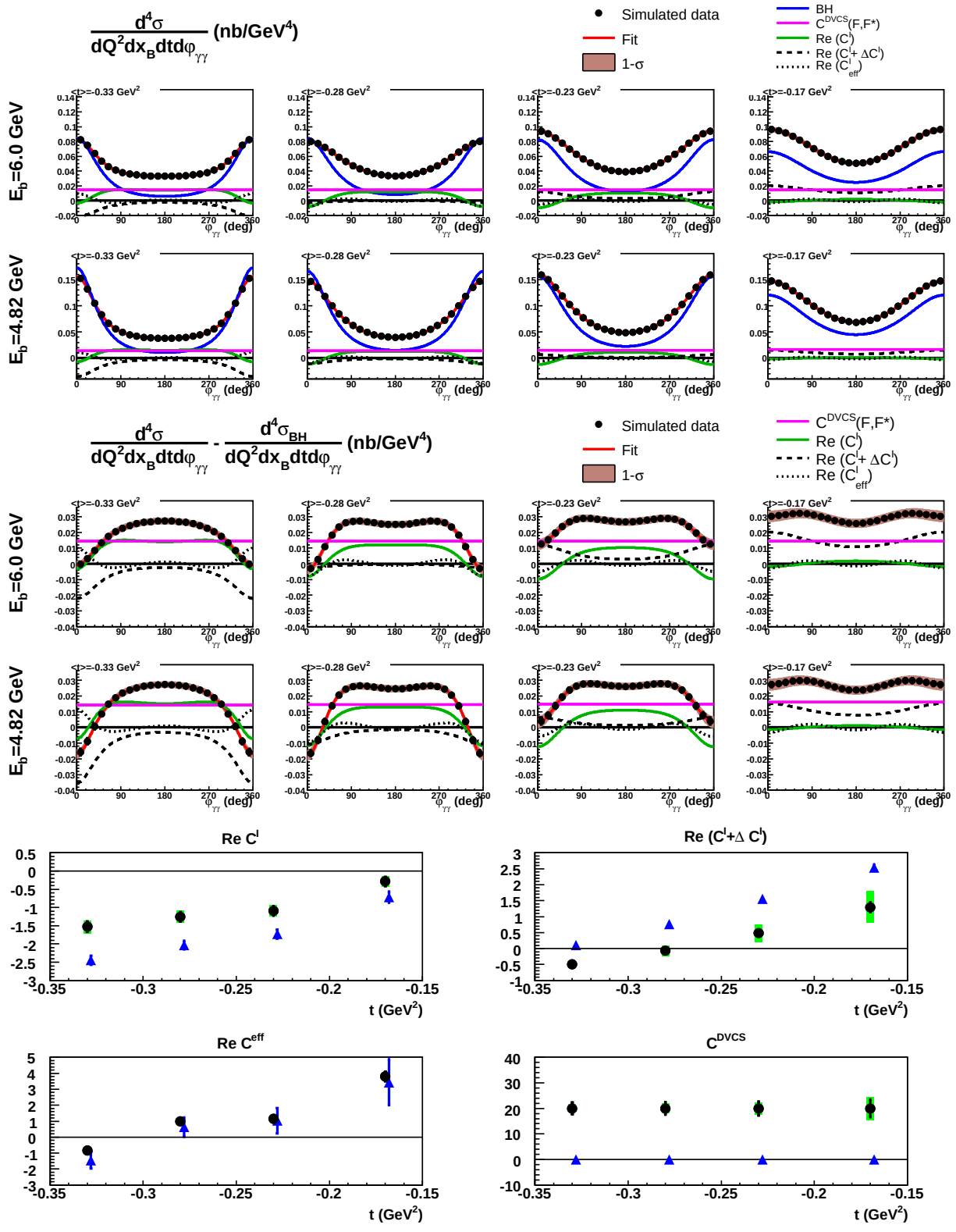

FIG. 10: Projected cross-section measurements for the $Q^2 = 1.9$ GeV^2 setting. $\mathcal{C}^{\rm DVCS}(\mathcal{F}, \mathcal{F}^*) = 20$ in this estimate. Bottom plots show the statistical (error bars) and the systematic (green boxes) uncertainties in each of the extracted (interference and DVCS^2) coefficients (black dots), compared to E00-110 extraction (blue triangles, slightly offset for visual clarity).

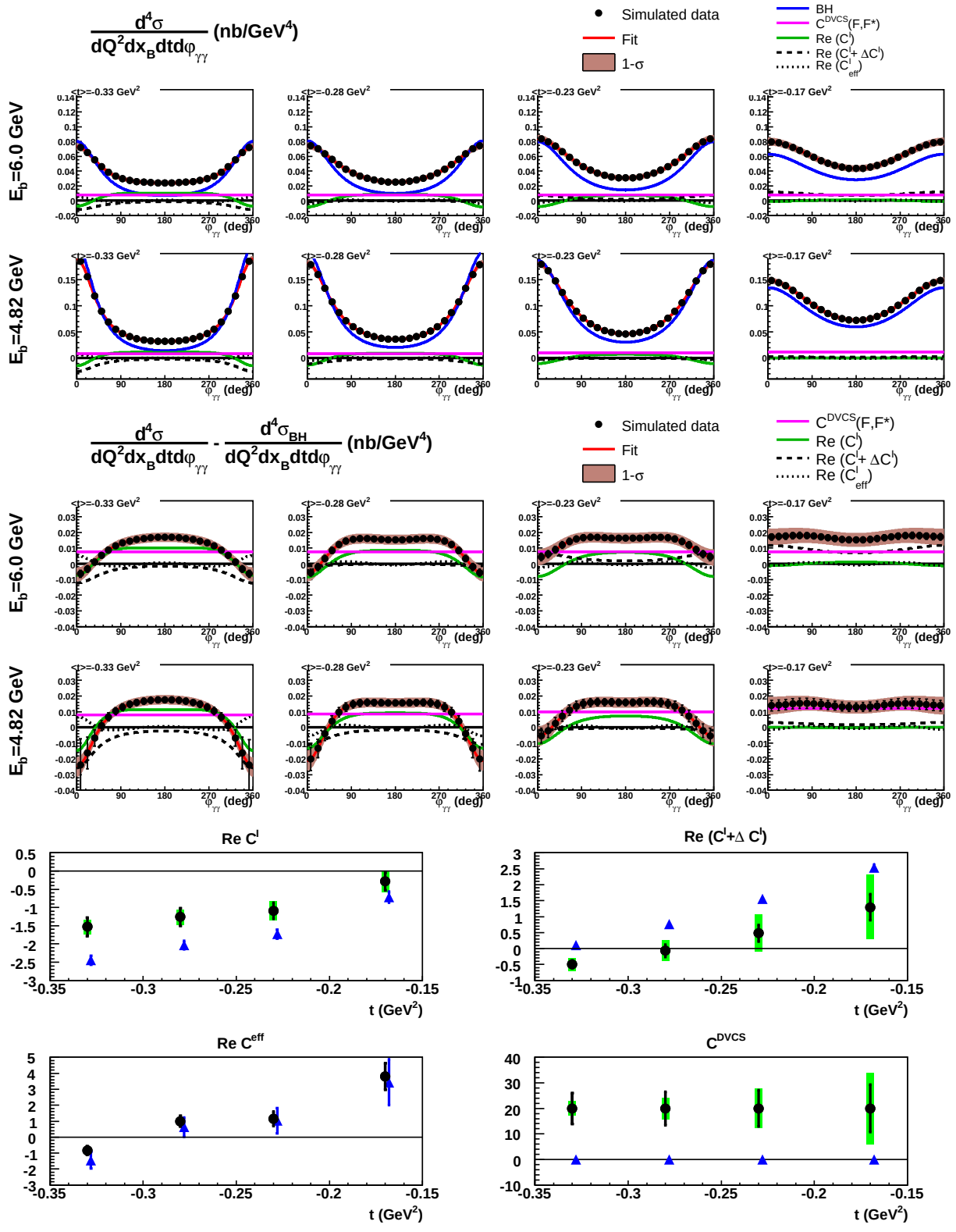

FIG. 11: Projected cross-section measurements for the $Q^2 = 2.3$ GeV^2 setting. $\mathcal{C}^{\rm DVCS}(\mathcal{F},\mathcal{F}^*) = 20$ in this estimate. Bottom plots show the statistical (error bars) and the systematic (green boxes) uncertainties in each of the extracted (interference and DVCS^2) coefficients (black dots), compared to E00-110 extraction (blue triangles, slightly offset for visual clarity).

In the cross-section plots of Figs. 9–11 error bars show the total uncertainty of the cross section measurement. Error bands show the uncertainty in the cross section by combining all different fitted contribution and *not* taking into account the correlations between the different contributions. The difference between the error bars and the error bands gives an idea of the correlation between the different fitted contributions. Only at high Q^2 the extracted coefficients show a slight correlation (i.e. error bars differ from the error band). This is especially true at smaller t, due to the more similar $\phi_{\gamma\gamma}-$dependence of the DVCS^2 and interference contributions.

Finally, let us note from Figs. 9–11 that:

- the coefficients $\Re\mathrm{e}C^I$,and $\Re\mathrm{e}(C^I + \Delta C^I)$ are extracted with error bars of smaller than ± 0.25. These coefficients are very different from the E00-110 phenomenological coefficients if the DVCS^2 term is large.

- the C^{DVCS} coefficient has an uncertainty of about ± 10 at high Q^2, but smaller than ± 2 at low Q^2 (the relative uncertainty will depend of its actual value).

- the coefficient $\Re\mathrm{e}C^{eff}$ which is twist-3 is not affected much by the potential large value of the DVCS^2 coefficient. This is particularly important since the conclusion that the twist-2 contribution is larger than twist-3 holds independent of the size of DVCS^2.

The accuracy on the extracted coefficients is better at lower Q^2. This is due to the fact that the relative contribution of the BH to the total cross section is smaller at lower Q^2. Since the extraction procedure relies on fitting the total cross section minus the BH contribution, the situation is improved at low Q^2.

In summary, the lever arm in beam energy of $\Delta k = 1.18$ GeV (for Q^2=1.9 and 2.3 GeV^2) and $\Delta k = 2.36$ GeV (for Q^2 =1.5 GeV^2) is enough to perform a meaningful separation of the DVCS^2, or, if this contribution is small, enough to draw a decisive conclusion about its size. This experiment is in a unique position to perform a full separation of the photon electroproduction cross section using this two-energy *Rosenbluth-like* method.

B. π^0 Rosenbluth separation

Because both the VGG and Laget models predict cross section values well below the cross section $d\sigma_T + \epsilon\, d\sigma_L$ we measured in E00-110, it is difficult to use these models in

order to get a reliable counting rate. In order to estimate the expected accuracy on the Rosenbluth separation of $d\sigma_L$ and $d\sigma_T$, we used the value of $d\sigma_T + \epsilon\, d\sigma_L$ we measured in E00-110 at $Q^2 = 2.3$ GeV^2 for all three Q^2=1.5, 1.9 and 2.3 GeV^2 in this new experiment. This estimate is then conservative, as exclusive cross sections are expected to increase as W decreases. Then, we chose three different values of the ratio $d\sigma_T : d\sigma_L = 2:1$, $1:1$, $1:2$. Fig. 12 and Fig. 13 show the expected uncertainties in the LT separation of the π^0 electroproduction cross sections for each of the three Q^2 settings and for each value of the ratio $d\sigma_T : d\sigma_L$.

Note that in addition to $d\sigma_L$ and $d\sigma_T$, we will measure also the three interference cross sections $d\sigma_{LT}$, $d\sigma_{TT}$ and $d\sigma_{LT'}$ as a function of Q^2. The statistical accuracy of these measurements will be a factor $\sqrt{2}$ better than in E00-110 (cf. Fig. 5) because we will double the statistics by using the two $\epsilon-$settings.

The systematic uncertainty of the π^0 (unseparated) cross section measurement will be at most of the same order as the systematics of the DVCS cross section measurements (cf. Tab. VII). Indeed, the π^0 channel is even more cleanly identified than DVCS thanks to the two-photon invariant mass.

VII. SUMMARY

With 400 h beam time (and 6 additional days for calibration and curing), this proposal will address an essential issue for GPD measurements for the 12 GeV upgrade program. Understanding the relative sizes of the different contributions to the DVCS cross section is a necessary step in order to extract reliable GPD information from data. The results of this experiment will provide accurate information that will help to plan and design the future and longer experiments for the upcoming 12 GeV experimental program.

In addition, the Q^2 dependence of the real part of the DVCS·BH interference terms and of the twist-2 DVCS^2 term in the helicity-independent cross section will provide supplementary tests of twist-2 dominance of the DVCS amplitude in the Q^2 range of this proposal. A measure of the size and Q^2 dependence of the separated $d\sigma_L/dt$ and $d\sigma_T/dt$ cross sections for deeply virtual π^0 electroproduction is an essential step towards understanding this reaction in terms of generalized parton distributions.

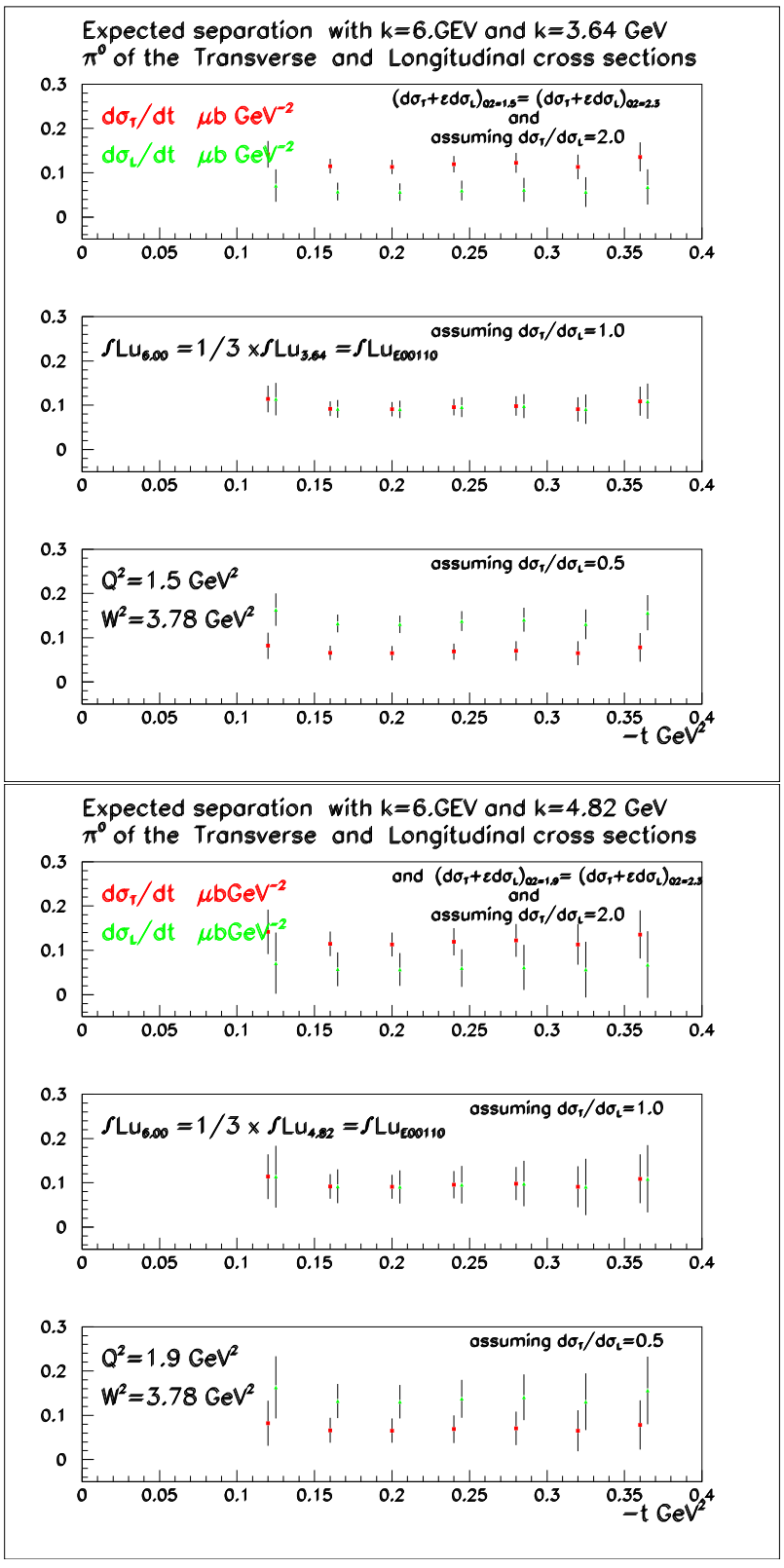

FIG. 12: Expected L/T separation for $Q^2 = 1.5\,\mathrm{GeV}^2$ (top) and $Q^2 = 1.9\,\mathrm{GeV}^2$ (bottom).

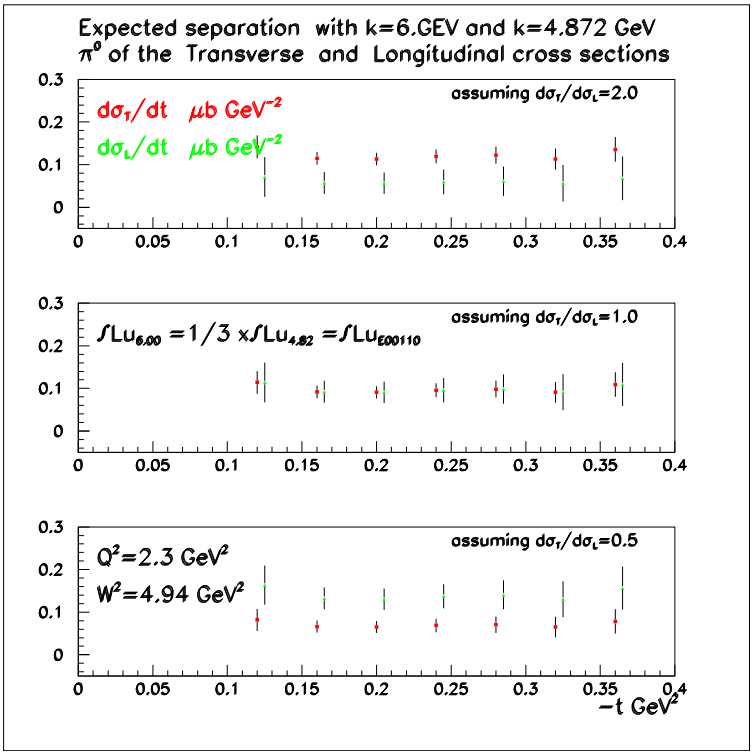

FIG. 13: Expected L/T separation for $Q^2 = 2.3\,\mathrm{GeV}^2$.

APPENDIX A: OPTICAL CURING OF THE CALORIMETER

The Hall A DVCS apparatus can run at very high luminosities especially thanks to the 1 GHz Analog Ring Sampler digitizer system. In such conditions, the PbF_2 crystal blocks of the calorimeter are irradiated and will accumulate doses that damage their transmission properties. Those effects result in a loss of energy resolution of the calorimeter that in turn can reduce the missing mass resolution. Achenbach *et al.* have reported that it is possible to cure this damage by exposing PbF_2 blocks to near UV blue light. This appendix describes the tests that we plan to do at the JLab-FEL in order to develop the optical curing for the Hall A DVCS calorimeter.

1. E00-110 Performance

The limiting factor for the instantaneous luminosity of the Hall A DVCS experiments is the pile-up rate within the 20 ns analysis window of the pulse shape analysis of the

PbF_2 signals. For each kinematic setting of this proposal , the instantaneous luminosity is calculated such that the simulated rate per PbF_2 block is no higher than in the successful data taking of E00-110 and E03-106. During the entire 80 days run of E00-110 and E03-106, a total of 12 Coulomb was delivered to the 15 cm liquid hydrogen and deuterium targets. Absolute calibrations of the PbF_2 calorimeter with elastic events (proton in HRS and electrons in the calorimeter) were performed at the beginning and end of data taking. Up to a 20% decrease in signal amplitude in individual blocks was measured, without observable loss in missing mass resolution after recalibration. Nevertheless, this amount of signal loss is the maximum we feel comfortable with to maintain optimal missing mass resolution. The 20% loss of amplitude is attributed to degradation of the transmission properties of the blocks, and not to degradation of the photo-cathodes of the PMTs, as custom pre-amplifiers were used to keep the PMT anode current small. PMT tests after the E00-110 experiment showed no significant degradation of their gain.

2. Radiation Dose Estimation

Radiation damage is determined by both instantaneous dose rate and integrated dose. Independent numerical [17] and analytic simulations indicate that the radiation dose absorbed by the calorimeter blocks at angles less than 10° is dominated by Moeller electrons (and related bremsstrahlung). It is therefore possible to estimate the dose absorbed by the blocks both during the completed E00-110 and E03-106 experiment and during the upcoming DVCS experiments. The dose absorbed by the blocks for the 12 GeV experiment is expected to be 10 times the dose absorbed during E00-110 and E03-106. One also notes that the average dose rates will be higher. For the experiment proposed to this PAC, the total dose is only 3 times larger than during E00-110 and E03-106 but with a dose rate 7 times larger.

Experiment	Dose (kRad)	Dose Rate (kRad/h)
E00-110 + E03-106	750	0.7
This proposal	2077	5.2
PR12-06-114	8406	4.9

TABLE VIII: Absorbed doses for the Hall A DVCS experiment calorimeter blocks that are the closest to the beam-line. The first column is the cumulated dose for the whole duration of the experiment while the second one is the average dose rate.

3. Radiation damage and optical curing

Achenbach *et al.* [18] studied the radiation damage of PbF_2 crystals from a ^{60}Co source. They obtained good results for curing the radiation damage by exposure to a Hg(Ar) pencil lamp (filtered to pass only $\lambda > 365$ nm). For a dose of 100 kRad, they observed a loss in transmission for blue light of 25%, which is comparable to the transmission loss observed during E00-110 and E03-106 but corresponds to a dose 7 times smaller than the one absorbed during the DVCS experiments. One possible explanation is that the ^{60}Co dose was recorded as a volumetric dose (1Gy = 1Joule/kg), yet the gamma rays from Cobalt are predominantly absorbed in a layer of thickness 1/10 the transverse size of the crystals. The radiation dose in Hall A during a DVCS experiment is primarily from photons and electrons with energy between 50 and 1000 MeV, which deposit energy more in the depth of the crystals. An other possible explanation is the difference of dose rate between the two cases. Achenbach test were performed with dose rate ranging from 20 to 150 kRad/h. A radiation hardness study of $PbWO_4$ (scintillating) crystal blocks of the BTeV experiment [19] showed that radiation damage depends on the dose rate (Rad/unit of time). As PbF_2 is a pure Cerenkov medium, we expect it to be less radiation sensitive than $PbWO_4$. However, we take the BTeV result as illustrative. In order to better understand the optical response of blocks to radiation dose, the performance of the optical curing procedure and the effect of repeated optical curing, we plan to perform the test detailed below in the Summer 2007.

4. FEL test

The upgraded JLab FEL produces over 10 kW of infrared light by wiggling a 160 MeV electron beam of intensity of the order of 10 mA [20]. The energy of the electrons makes the FEL an ideal instrument to produce electromagnetic showers comparable to the ones produced by Moeller electron during the Hall A DVCS experiment, typically ranging from 50 down to 10 MeV. With little re-configuration of the beam line [21], it is possible to use the electron beam to irradiate a sample of the DVCS PbF_2 crystals. For example, a 100 MeV electron beam scattering off a carbon target will produce a fan of quasi monochromatic electrons by elastic scattering. With a 1 μA beam incident on a 1.7 g/cm^2 target, elastic scattering will produce a dose rate of 60 kRad/h in a DVCS PbF_2 block located a meter from the target at 5° to the beam line. The same conditions will produce a dose rate of 3 kRad/h for a block at 10°. Our plan is to locate a dozen or so block at different angles with respect to the beam line, in order to irradiate them at different dose rates. Over the course of roughly one week, two hours of daily irradiation (in the evenings, when the FEL is not in use for light generation) will be followed by transmission measurement (expected to last 15 min per block). Each time a block is observed to lose 20% of its initial transmission, it will be exposed to blue light curing (approximately 17 hours), followed by transmission measurements and new irradiation.

In conclusion, we plan to use the JLab-FEL to develop our optical curing method of the radiation damage of the calorimeter block. This facility can provide an electromagnetic flux of variable intensity with a spectrum comparable to the background irradiation of the calorimeter blocks in the DVCS experiment. Thus the FEL is perfectly suited to our study.

APPENDIX B: KINEMATIC DISTRIBUTIONS

Fig. 14 shows the distributions of several relevant kinematic variables for each Q^2 setting, with the distributions for each beam energy superposed. The DIS variables x_B, ν, Q^2 show good overlap, with essentially symmetric discrepancies in coverage of x_B and Q^2. The variable ϵ is the usual virtual photon polarization parameter, and illustrates the lever arm for L/T separations of the π^0 cross sections, as presented in section VI B. The DVCS variables $t = (q - q')^2$, polar angle $\theta_{\gamma\gamma^*}$ of the detected photon relative to the **q**-vector, and the azimuthal angle $\phi = \phi_{\gamma\gamma}$ of the detected photon around the **q**-vector, also show good consistency at the two beam energies. The oscillations in the ϕ distributions at $Q^2 = 1.5$ GeV^2 setting reflect the variations in the acceptance at the largest t-bin, resulting from the shape of the calorimeter. We note that at the highest Q^2 point, the expanded calorimeter will have a much large acceptance in t than just the specific bins we have presented for the full Q^2-dependent studies.

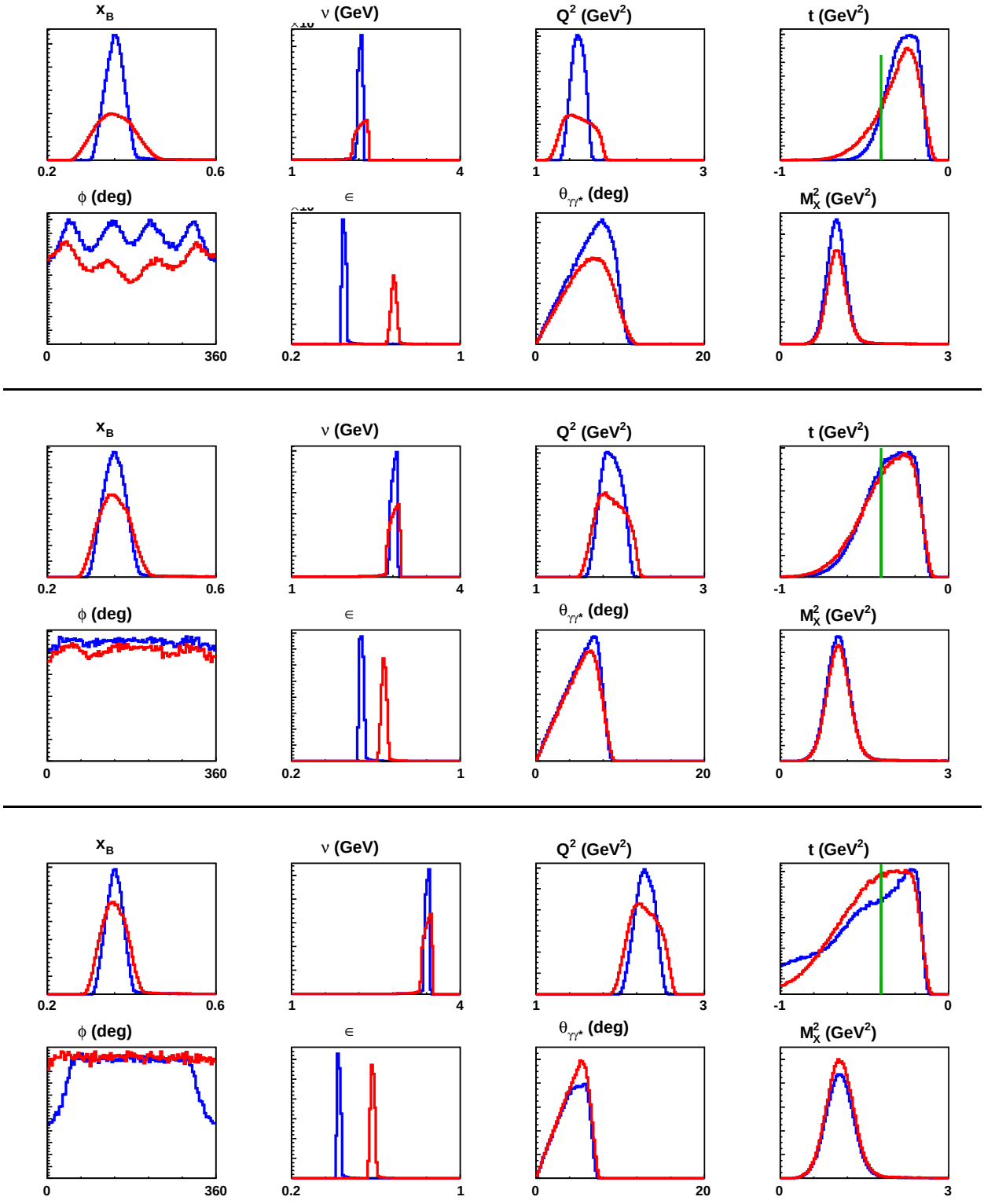

FIG. 14: Kinematic spectra for each Q^2 setting (from top to bottom: Q^2 = 1.5, 1.9, 2.3 GeV^2) and each beam energy (red: E_b =6 GeV; blue: E_b =4.82 or 3.64 GeV). A cut on $-t < 0.4$ GeV^2 (green line) has been applied to all histograms, except to the $t-$histograms.

REFERENCES

[1] C. Muñoz Camacho et al. (Jefferson Lab Hall A), to appear in Phys. Rev. Lett. (2006), nucl-ex/0607029.

[2] X.-D. Ji, Phys. Rev. Lett. **78**, 610 (1997), hep-ph/9603249.

[3] D. Mueller, D. Robaschik, B. Geyer, F. M. Dittes, and J. Horejsi, Fortschr. Phys. **42**, 101 (1994), hep-ph/9812448.

[4] M. Diehl, T. Gousset, B. Pire, and J. P. Ralston, Phys. Lett. **B411**, 193 (1997), hep-ph/9706344.

[5] A. V. Belitsky, D. Mueller, and A. Kirchner, Nucl. Phys. **B629**, 323 (2002), hep-ph/0112108.

[6] K. Goeke, M. V. Polyakov and M. Vanderhaeghen, Prog. Part. Nucl. Phys. **47**, 401 (2001).

[7] M. Guidal, M. V. Polyakov, A. V. Radyushkin, M. Vanderhaeghen, Phys. Rev. **D72**, 054013 (2005).

[8] M. Vanderhaeghen, P. Guichon and M. Guidal, Phys. Rev. **D60**, 094017 (1999).

[9] M. Diehl, Eur. Phys. J. **C25**, 223 (2002), hep-ph/0205208.

[10] J. P. Ralston and B. Pire, Phys. Rev. **D66**, 111501 (2002), hep-ph/0110075.

[11] C. Woody et al., IEEE Trans. Nucl. Sci. **40**, 546 (1993).

[12] D. F. Anderson, J. A. Kierstead, S. Stoll, C. L. Woody, and P. Lecoq, Nucl. Instrum. Meth. **A342**, 473 (1994).

[13] F. Feinstein, Nucl. Instrum. Meth. **A504**, 258 (2003).

[14] J. Roche, C. E. Hyde-Wright, B. Michel and C. Muñoz Camacho (spokespersons), PR12-06-114, approved by PAC30 (2006), nucl-ex/0609015.

[15] M. Rvachev, Hall A Technical Note Jlab-TN-01-055, Jefferson Lab (2001), URL `http://hallaweb.jlab.org/publications/Technotes/technote.html`.

[16] M. Vanderhaeghen, J. M. Friedrich, D. Lhuillier, D. Marchand, L. Van Hoorebeke, and J. Van de Wiele, Phys. Rev. **C62**, 025501 (2000), hep-ph/0001100.

[17] P. Degtiarenko (2006), private communication, URL `www.jlab.org/~pavel/cehw`.

[18] P. Achenbach et al., Nucl. Instrum. Meth. **A416**, 357 (1998).

[19] V. A. Batarin et al. (BTeV electromagnetic calorimeter group), Nucl. Instrum. Meth. **A512**, 488 (2003), hep-ex/0210011.

[20] G. Neil et al., Nucl. Instrum. Meth. **A557**, 9 (2006).

[21] G. Krafft (CASA/JLab) (2006), private communication.

[22] E03-106 is the DVCS experiment on the neutron that immediately followed E00-110.

[23] Due to the small (around 7%) beam spin asymmetry of the π^0 electroproduction channel (cf. Fig. 4), the uncertainty introduced to the DVCS helicity-dependent cross section is smaller than to the helicity-independent cross section.